NeuroImage 202 (2019) 116090

Contents lists available at ScienceDirect

NeuroImage

journal homepage: www.elsevier.com/locate/neuroimage

A systematic optimization of ^{19}F MR image acquisition to detect macrophage invasion into an ECM hydrogel implanted in the stroke-damaged brain

Harmanvir Ghuman [a,b], T. Kevin Hitchens [c], Michel Modo [a,b,d,*]

[a] McGowan Institute for Regenerative Medicine, University of Pittsburgh, Pittsburgh, PA, USA
[b] Department of Bioengineering, University of Pittsburgh, Pittsburgh, PA, USA
[c] Department of Neurobiology, University of Pittsburgh, Pittsburgh, PA, USA
[d] Department of Radiology, University of Pittsburgh, Pittsburgh, PA, USA

ARTICLE INFO

Keywords:
^{19}F MRI
Perfluorocarbon
Macrophage
Brain
Hydrogel
Stroke
Acquisition
Sequence
Optimization
Nanoemulsion

ABSTRACT

^{19}F-MR imaging of perfluorocarbon (PFC)-labeled macrophages can provide a unique insight into their participation and spatio-temporal dynamics of inflammatory events, such as the biodegradation of an extracellular matrix (ECM) hydrogel implanted into a stroke cavity. To determine the most efficient acquisition strategy for ^{19}F-MR imaging, five commonly used sequences were optimized using a design of experiment (DoE) approach and compared based on their signal-to-noise ratio (SNR). The fast imaging with steady-state precession (FISP) sequence produced the most efficient detection of a ^{19}F signal followed by the rapid acquisition with relaxation enhancement (RARE) sequence. The multi-slice multi-echo (MSME), fast low angle shot (FLASH), and zero echo time (ZTE) sequences were significantly less efficient. Imaging parameters (matrix/voxel size; slice thickness, number of averages) determined the accuracy (i.e. trueness and precision) of object identification by reducing partial volume effects, as determined by analysis of the point spread function (PSF). A 96×96 matrix size (0.35 mm^3) produced the lowest limit of detection (LOD) for RARE (2.85 mM PFPE; 119 mM ^{19}F) and FISP (0.43 mM PFPE; 18.1 mM ^{19}F), with an SNR of 2 as the detection threshold. Imaging of a brain phantom with PFC-labeled macrophages invading an ECM hydrogel further illustrated the impact of these parameter changes. The systematic optimization of sequence and imaging parameters provides the framework for an accurate visualization of ^{19}F-labeled macrophage distribution and density in the brain. This will enhance our understanding of the contribution of periphery-derived macrophages in bioscaffold degradation and its role in brain tissue regeneration.

1. Introduction

Immune cells participate in pro-inflammatory and pro-repair activities, but understanding their trafficking to sites of injury and repair remains a major challenge (Ogle et al., 2016; Valentin et al., 2009). Histological time course studies are impeded by focusing on a limited number of individual time points and require excision of small tissue samples for analysis. Although histological studies are essential to understand the local microscopic immune cell participation in these processes, complimentary longitudinal non-invasive imaging can provide important *in vivo* measurements of immune cell trafficking and system dynamics (Ahrens and Bulte, 2013; Ahrens et al., 2011; Flogel et al., 2008; Kadayakkara et al., 2012; Srinivas et al., 2007; Zhong et al., 2015).

By exploiting the phagocytic activity of blood-circulating immune cells, such as peripheral macrophages, contrast agents or tracer material can be incorporated into cells to non-invasively visualize their *in vivo* distribution by MRI (Ahrens and Zhong, 2013; Gaudet et al., 2017; Jacoby et al., 2014). Although supra-paramagnetic iron oxide (SPIO) nanoparticles are often used for cellular MR imaging of the mononuclear phagocyte system (MPS) due to their high sensitivity (Bulte and Frank, 2000), the image hypointensity produced by SPIO interferes with T_2-weighted analyses and other MRI measures (e.g. perfusion, diffusion), which can offer valuable information to characterize the lesion onset, evolution and repair (Modo et al., 2005). Alternatively, systemic perfluorocarbon (PFC) labeling of immune cells can visualize *in vivo* cell trafficking using hetero-nuclear ^{19}F MRI without interfering with

* Corresponding author. University of Pittsburgh, McGowan Institute for Regenerative Medicine, 3025 East Carson St, Pittsburgh, PA, 15203, USA.
E-mail address: mmm154@pitt.edu (M. Modo).

https://doi.org/10.1016/j.neuroimage.2019.116090
Received 11 April 2019; Received in revised form 6 August 2019; Accepted 8 August 2019
Available online 10 August 2019

anatomical (^{1}H) imaging (Ahrens et al., 2005; Bonner et al., 2015; Hitchens et al., 2011; Jacoby et al., 2014). Although its sensitivity can be significantly lower than SPIO-labeled macrophages, the ^{19}F signal is detected directly and readily quantifiable due to its unique signal, as well as a lack of a physiological background signal (Temme et al., 2012). This "hot spot" imaging (Bulte, 2005) has been first reported 30 years ago (Ratner et al., 1987) and is increasingly used to investigate immune cell trafficking (Ahrens and Bulte, 2013).

Although ^{19}F-MR imaging has been used widely to visualize macrophages in peripheral tissues, only a few studies demonstrated the utility of this approach in the brain (Flogel et al., 2008; Mastropietro et al., 2014; Temme et al., 2012; Waiczies et al., 2013; Zhong et al., 2013b, 2015). The more limited invasion of circulating immune cells and richer anatomical detail of the brain pose additional imaging challenges, considering the lower sensitivity of ^{19}F imaging (Waiczies et al., 2013). A variety of sequences have been used for ^{19}F-MR imaging, but it remains unclear which sequence provides the most efficient acquisition strategy at a high magnetic field (9.4T) used for animal imaging (Anisimov et al., 2017; Colotti et al., 2017; Goette et al., 2015a, 2015b; Gong et al., 1991; Mastropietro et al., 2014; Taylor et al., 2016). To address this question, 5 commonly used sequences for ^{19}F-MR imaging (1. fast low angle shot, FLASH; 2. Multi-slice multi-echo spin-echo sequence, MSME; 3. rapid acquisition with relaxation enhancement, RARE; 4. zero echo time, ZTE; 5. fast imaging with steady-state precession, FISP) were optimized using a design of experiment (DoE) approach and compared based on signal-to-noise ratio (SNR), while keeping imaging time constant.

Once key sequence parameters (i.e. relaxation-time, echo-time, bandwidth, flip-angle) were optimized, other imaging parameters (i.e. number of averages, matrix size, slice thickness) were arrayed from a low to high values to establish detection limits. As ^{19}F-MR imaging generally achieves a relatively low image resolution, with hot spots of labeled immune cells compared to neuroanatomical structures in the brain (Zhong et al., 2015), we investigated the potential for partial volume effects in phantoms and how these artifacts can be minimized using reasonable imaging times (Alavi et al., 2018). We further determined the potential to resolve individual hot spots using a point spread function (PSF) that compared full width half maximum (FWHM) (Robson et al., 1997), as well as the contrast and distance between hot spots of different size, akin to approaches used to characterize positron emission tomography (PET) hot spot imaging (Hoffman et al., 1979; Kessler et al., 1984).

To illustrate the impact of different ^{19}F acquisition strategies on the detection of immune cells participating in brain tissue regeneration, we applied these acquisition parameters to image a rat head sample containing PFC-labeled immune cells that invaded an extracellular matrix hydrogel within 24 h after implantation into a stroke lesion (Ghuman et al., 2016, 2018). Although histology can provide very detailed information about the invasion of immune cells into the ECM hydrogel (Ghuman et al., 2016), it does not afford the visualization of the dynamic trafficking of cells from the blood compartment to the peri-infarct area, or the time course of ECM infiltration. At present, time-consuming cross-sectional studies are required to understand this relationship between immune cell infiltration and ECM biodegradation (Ghuman et al., 2018). ^{19}F-MR imaging of immune cell activity can overcome these shortcomings of histological studies (Ahrens and Bulte, 2013) and provide a complimentary *in vivo* tool to map the longitudinal interaction of immune cells with biomaterials to investigate their contribution to bioscaffold degradation and participation in tissue regeneration.

2. Materials and methods

2.1. Perfluorocarbon nanoemulsion

A commercially available perfluorocarbon (PFC) nanoemulsion V-Sense (VS-1000H, CelSense, Pittsburgh PA) was used as a probe for ^{19}F MR imaging sequence optimization. V-sense is formulated for direct i.v. injection in animals for *in situ* macrophage labeling and ^{19}F-MR inflammation hotspot imaging. The emulsified PFC has 165 nm diameter droplets of a perfluoropolyether (PFPE) with repeating subunits of $-(CF_2CF_2O)n-$, where $n = 10.5$ on average, producing an average molecular weight of 1380 g/mol (Janjic et al., 2008). The NMR spectrum consists of one major resonance peak at −91.55 ppm which accounts for ~42 fluorine (^{19}F) atoms per molecule and two minor peaks at −58.93 and −93.5 ppm. The 20% vol/vol preparation (360 mg PFPE/mL) yields a PFPE concentration of 260 mM with a ^{19}F atom concentration for the major peak of 10.92 M, as indicated by the manufacturer's description.

2.2. Preparation of PFC phantoms

For sequence optimization, a ^{19}F phantom was prepared by filling eight glass micro-pipet capillaries with PFC nanoemulsions to detect different log10 concentrations (0, 0.02, 0.2, 2, 10, 20, 100, 200 mM, $n = 3$/concentration) (Supplementary Fig. 1A). The capillaries were sealed at both ends and embedded in a 50 mL conical tube containing 2% agarose in H_2O. A separate phantom was prepared for resolving ^{19}F hot spots. For this, glass capillary tubes (Fisher Scientific) with inner diameters of 0.4, 0.9, and 1.8 mm were filled with 100 mM PFC and placed 0.5, 1, and 1.5 mm apart (Supplementary Fig. 1B).

2.3. ^{19}F MR imaging set-up

^{1}H- and ^{19}F-MRI was performed on two PFC phantoms and one perfusion-fixed rat head *ex vivo* using a 9.4T horizontal bore Bruker AVANCE AV3 HD MR scanner and a 40 mm (^{1}H/^{19}F) double resonance coil (Bruker, Billerica, MA) operating at 400.13 MHz and 376.46 MHz for ^{1}H and ^{19}F measurements, respectively. All images were acquired at ambient bore temperature (20 °C). After acquisition of ^{1}H images for phantom geometry/anatomy, morphologically matching ^{19}F images were acquired. The field of view (FOV), slice geometry, and slice thickness were identical for both ^{1}H and ^{19}F images to allow image overlay and segmentation.

2.4. ^{19}F MRI sequences optimization

A variety of sequences were utilized for ^{19}F image acquisition. We compared five commonly used sequences to define the most sensitive image acquisition for visualizing PFC nanoemulsions: 1) FLASH; 2) MSME; 3) RARE; 4) ZTE); 5) FISP. To define optimal imaging parameters, a design-of-experiment (DoE) approach was implemented. Key acquisition parameters were arrayed from a low to high value: 1) repetition-time (TR); 2) echo-time (TE); 3) bandwidth; and 4) flip-angle. DOE experiments investigated interactions between parameters and afforded the computation of contour maps to cover experimental space. This then afforded the selection of optimal parameters based on the central values of the highest SNR.

2.5. Signal-to-noise ratio (SNR) and detection limit

To calculate SNR, ROIs were drawn around the areas in the phantom containing the PFC nanoemulsion (i.e. signal) and an ROI was drawn in the surrounding agarose to define the noise. Commonly in MR imaging, SNR is defined as the mean signal intensity divided by the standard deviation of the noise (Supplementary Fig. 2A) (Welvaert and Rosseel, 2013). However, the noise in magnitude MR images is characterized by a Rician distribution (Gudbjartsson and Patz, 1995), and the use of a standard deviation, a property of normally distributed data, is inappropriate. In some cases, look-up tables (Bouchlaka et al., 2016; Srinivas et al., 2007) or scaling factors (Taylor et al., 2016; Waiczies et al., 2017) have been applied to "correct" the SNR, but we did not use this convention here. Using the conventional definition of SNR ($\overline{S} / N_{SD}$), values of 3 (Flogel et al., 2008; Meissner et al., 2015; Partlow et al., 2007), 3.5 (Boehm-Sturm et al., 2011; Mastropietro et al., 2014; Taylor

et al., 2016) or 4 (Colotti et al., 2017) have previously been suggested as detection limits for ^{19}F imaging (Taylor et al., 2016). However, the lower standard deviation of the noise due to the Rician distribution can increase computed SNR, especially when noise and signal values are close to each other. We therefore here used the mean noise intensity ($\overline{N}$), rather than standard deviation (N_{SD}), as divisor to avoid introduction of a calculating bias in concentrations below detection threshold (Supplementary Fig. 2B). An SNR ($\overline{S}$ / $\overline{N}$) of 1 hence indicates a "signal" equivalent to noise. However, once SNR is calculated, these measures follow a normal distribution and afford parametric comparisons. A 25% increase (Bible et al., 2012) of the signal or 1 standard deviation (Meissner et al., 2015) above the mean noise have also been used to define the ^{19}F detection threshold, irrespective of the intensity distributions.

To define an appropriate SNR as a detection threshold, a whole rat head with PFC-labeled macrophages was used to measure voxels with variable PFC content to map signal distribution and compare this to the ^{19}F noise distribution. Intensity measures were binned for every 5-point increment. Distribution curves were defined using the locally weighted scatterplot smoothing (LOWESS) regression analysis. The mean, mode, median, standard deviation and intersection point for distributions were determined using Prism 8 (GraphPad). Type 1 and Type 2 error rates were calculated. Different detection thresholds (SNR = 1, 2, 3; 10, 25 and 35% signal above noise) were illustrated to define an appropriate value for detection sensitivity. A limit of detection (LOD) was determined by measuring SNR of different concentrations of VS1000H (PFPE) (0, 0.02, 0.2, 2, 10, 20, 100, 200 mM, n = 3/concentration) with optimized sequences. An SNR of 2 was defined as the detection threshold that affords a calculation of the LOD concentration. Two key variables affect ^{19}F imaging sensitivity: 1) voxel size (i.e. how much signal is present within a voxel); 2) signal averaging (i.e. time).

2.6. Partial volume effects

Partial volume effects in hot spot imaging occur when the signal area is smaller than the voxel size (Supplementary Fig. 2C). The signal can be below the detection threshold and lead to a false negative, but the signal can also be very high and lead to a spill-over effect into neighboring voxels, which can also occur when voxel size is relatively large. Partial volume loss can occur when the signal of the hot spot is divided across multiple voxels, which could occur when voxel size is smaller than the imaged object. Spill-out effects in this case can occur, where voxels neighboring the large object have insufficient signal to reach the detection threshold. In ^{19}F imaging of macrophages, it is expected that $>10^3$-10^4 PFC-labeled cells are required to be present in a single voxel to achieve the detection threshold with individual voxel signal intensity related to the number of macrophages and cell loading (Supplementary Fig. 2D). Signal division of a single object across multiple voxels, as well as spill-out effects, are therefore unlikely. However, partial volume effects due to not reaching the detection threshold or spill-over effects due to a large number of macrophages being localized within a voxel are likely.

To address, these issues, we investigated the impact of scanning time (1 average, 15 min, 30 min, 60 min, 120 min), matrix size (32 × 32 to 128 × 128) and slice thickness (1–2 mm) on SNR to define imaging parameters that reduce potential partial volume effects, while achieving a sufficient detection of small macrophage clusters in the stroke-damaged brain. This approach allowed us to define which sequence achieves a sufficient SNR (>2) for the smallest possible voxel volume within a 60 min scan.

2.7. Point spread function and distinction of hot spots

Partial volume effects can also affect the separation of hot spots. Signals within a voxel will produce an axial and lateral point spread function (PSF), which defines the localization of the ^{19}F signal (Supplementary Fig. 1F). To define clusters of cells, it is hence important to achieve a sufficient spatial resolution in-plane, as well as to ensure that slices are sufficiently thin to resolve their anatomical location (Supplementary Fig. 1G). PSF for symmetrically circular objects can be calculated based on a single line spread function that is drawn across the diameter of the object (Smith, 1997). Distinction of two hot spots is dependent on a separation of their PSF. In the case of both hot spots being undistinguishable from each other, the PSFs for both are unresolved (Supplementary Fig. 1H). Improvements in distinguishing hot spots are dependent on further separation of PSFs, as defined by the Sparrow, Abbe and Rayleigh limits. Fully resolved PSFs will produce a region of noise between hot spots to achieve full contrast.

Full width at half maximum (FWHM) is commonly used to measure the point separation and signal contrast. For this, straight lines passing through the middle of capillaries were drawn as ROIs to obtain a ^{19}F intensity profile as a function of distance (in mm). FWHM was calculated by measuring the distance between half maxima (intensity maximum/2) for each PSF (Supplementary Fig. 1I). Point separation measured the distance between half maxima of the adjacent PSFs (Supplementary Fig. 1J). Contrast was defined as the difference between maximum and minimum intensity measured between two PSFs. FWHM and point separation were expressed as absolute error (actual – measured).

2.8. Ex vivo ^{19}F MR imaging of rat head with PFC-labeled macrophages

To illustrate the impact of different acquisition parameters on mapping the distribution of PFC-labeled macrophages invading an ECM hydrogel implanted into a stroke cavity (Ghuman et al., 2016, 2018), a head sample was prepared and scanned using the same parameters.

Middle cerebral artery occlusion. To model stroke, a rat (Sprague-Dawley) was anesthetized using isoflurane (4% induction, 1.5% maintenance) to insert a thin 0.37 mm filament (Doccol) into the internal carotid artery to perform middle cerebral artery occlusion (MCAo) for 70 min (Modo et al., 2000). For reperfusion of the MCA, the animal was re-anesthetized and the filament was drawn back to the carotid bifurcation. Extensive post-operative care was provided with Buprenex (0.05 mg/kg i.p.) given twice daily for 3 days to alleviate pain from the surgical intervention (Bible et al., 2009; Modo et al., 2000).

Tagging macrophages with PFC. Equal volumes of VS-1000H and VS-1000H DM Red were used to label macrophages 24 h before ECM implantation. For this, the animal (320 g) was anesthetized using isoflurane and a single tail vein injection of PFC (1200 mg/kg; 3.33 mL/kg) was administered to the animal. This achieves a reported labeling efficiency of 50% for peripheral monocytes/macrophages (Flogel et al., 2008).

Extracellular matrix (ECM) hydrogel implantation. De-cellularization of tissues and their formulation as scaffold material has been extensively described (Badylak et al., 1999, 2009; Badylak, 2004; Crapo et al., 2011; Medberry et al., 2013). To ensure complete coverage of the lesion volume at a defined protein concentration, ECM pre-gel (4 mg/mL, MatriStem powder, ACell, Columbia MD) was injected into the stroke cavity using an injection-drainage approach that defined injection volume and sites using T_2-weighted MR images (RARE, 5000/40 ms TR/TE, 40 × 40mm FOV, 192 × 192 matrix, 0.208 mm in-plane resolution, slice thickness 1.5 mm) of the stroke lesion (Massensini et al., 2015). A pre-gel volume equivalent to the lesion cavity was injected using a 250 μL Hamilton syringe with a 24G needle, while extracellular fluid from the cavity was drained through a cannula (Massensini et al., 2015).

Ex vivo ^{19}F imaging for macrophage detection. The rat was perfusion-fixed under terminal anesthesia (1 mL/kg Fatal-plus) using 4% paraformaldehyde at 24 h post-implantation. *Ex vivo* MRI consisted of a T_2-weighted scan to visualize the lesion cavity and place the ^{19}F signals into anatomical context. ^{19}F-MR images were acquired with all sequences used in the phantom studies to highlight the impact of scanning time, voxel volume, and slice thickness. Individual images were thresholded at

an SNR = 2 to visualize the ^{19}F signal.

2.9. Statistical analysis

Although the ^{19}F signal did not exhibit a normal distribution, SNR measures did and hence afforded parametric statistical analyses. Comparisons of a single independent and dependent variable were analyzed using one-way ANOVAs followed by Bonferroni's post-hoc test. In the case of two independent variables (e.g. sequence and PFC concentration), two-way ANOVAs were used. Statistical significance was set at $p < 0.05$. Statistical analyses and graphing of data were performed in Prism 8 (GraphPad, San Diego, CA). To illustrate the interactions between two independent variables, contour maps were computed (Minitab, State College, PA) with SNR as the dependent variable. To afford comparisons across all sequences, contour lines were defined by 6 equal data ranges (bin sizes) that spanned the measured value range.

3. Results

3.1. Defining a detection threshold based on SNR

To empirically define SNR and an appropriate detection threshold, a head sample with PFC-labeled macrophages invading an ECM bioscaffold implanted after a stroke was acquired using a FISP sequence and a matrix size of 96 × 96 (Fig. 1A). The image was segmented into head (31.4% of voxels), noise (65%), ECM implantation area with PFC-labeled macrophages (2.46%) and the positive control (1.15%) consisting of a vial with 100 mM of PFPE (VS1000H). The PFC-labeled macrophage region was used to map the ^{19}F distribution, rather than the positive control, as its uniform signal produces a signal that is not representative of ^{19}F imaging. Mapping the signal intensity distribution indicated a Rician distribution for ^{19}F background noise and a bimodal distribution of the ^{19}F signal (Fig. 1B). Descriptive statistics of both distributions further indicated that the mode, mean and median differed markedly. Both distributions were skewed (normal = 0) and showed marked Kurtosis (normal = 3) (Fig. 1C). Neither distribution followed a normal Gaussian distribution curve, as indicated by significant deviations from normality.

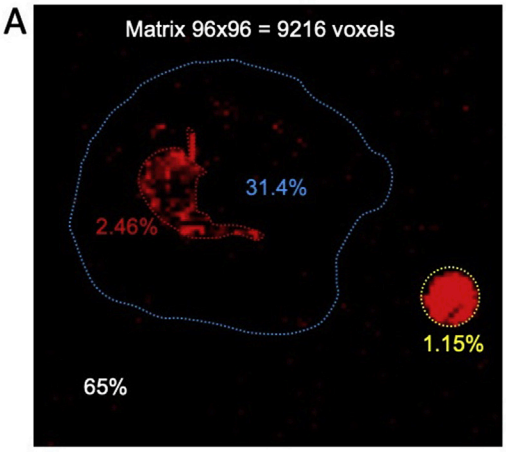

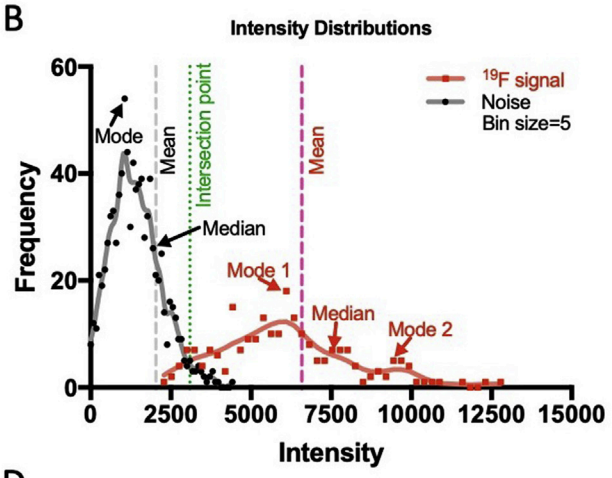

C

Statistic	Noise	^{19}F Signal
Voxel n	885	227
Mean	2032	6582
Median	1944	7537
Mode	1060	1: 6104 2: 9448
SD	768	1992
Skewness	0.52	1.045
Kurtosis	0.91	0.69
D'Agostino & Pearson	6.729*	9.62**
Shapiro-Wilk	0.9084***	0.8772***
KS normality	0.1479**	0.1738***

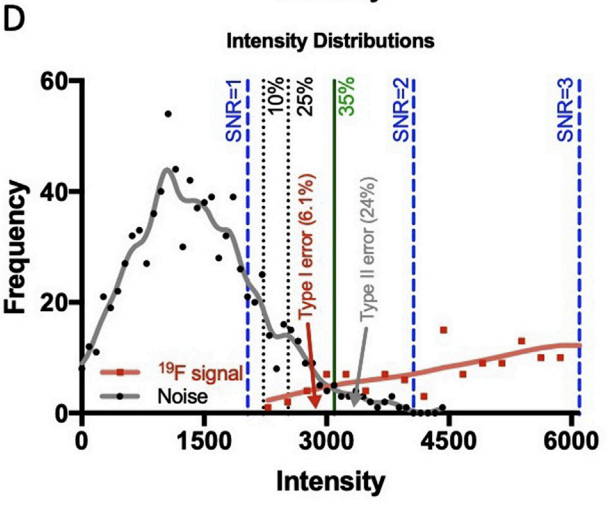

Fig. 1. Defining a detection threshold. A. Within an image slice, the vast majority (65%) of voxels are noise that is outside the skull, excluding a positive control (1.15%) PFC sample of known concentration (100 mM) used for standardization. Only 2.46% of all voxels are within the territory of macrophage invasion with ^{19}F positive voxels of different concentrations that require a distinction from the background noise signal. **B.** Plotting of the noise and ^{19}F signal intensity value reveals an overlap between these distributions. Noise follows a Rician distribution cut off by 0 with a high frequency of signal intensities that define the unimodal distribution. Bin sizes of 5 were defined for plotting the frequencies of signal intensities. The ^{19}F distribution is flatter due the lower number of positive voxels and follows a bimodal distribution. **C.** Descriptive statistics for noise and ^{19}F signals, including normality tests. **D.** A detection threshold is defined based on its ability to separate noise from signal, while reducing type I and type II errors. Based on the means of both distributions, a conservative detection threshold of 2 was retained that minimizes type II errors (i.e. identifying noise as signal) to <1%. This also accounts for some low intensity ^{19}F voxels potentially being noise rather than signal.

There was an overlap of both distributions with the intersection point, defining type I and type II errors (Fig. 1D). Type I errors indicate the risk of a false positive, i.e. identifying voxels containing ^{19}F signaling, but it is background noise. This error, using the intersection point to define a detection threshold, was at 6.1%. Conversely, the intersection point produced a 24% type II error, where noise signal could be mistaken for ^{19}F signal. An SNR calculated from the mean of the noise divided by the standard deviation of the noise would produce an SNR ($\overline{S}/N_{SD}$) of 2.64. However, the use of means would produce an SNR ($\overline{S}/\overline{N}$) of 1, when no signal is detected. Mean of noise is also below the level of any ^{19}F signal and hence would not produce a false positive or negative. SNR was hence calculated based on signal means. Using this SNR definition, an SNR of 2 will produce a conservative detection threshold that should not contain any noise contribution. Signal thresholds of 25% above noise would produce a significant number of false positives. The intersection point (52% above the mean of the noise) is almost within accepted limits of type I (5%) and type II (20%) errors. A detection threshold of a SNR = 3 would underestimate the actual ^{19}F signal and produce a large number of false negatives. We therefore here used an SNR ($\overline{S}/\overline{N}$) of 2 as our detection threshold.

3.2. DOE approach defines optimal sequence parameters

MRI sequences for ^{19}F imaging were optimized by arraying key parameters (TR, TE, bandwidth, flip angle) on a PFC phantom to measure SNR (see Table 1). These measurements were made at 9.4 T with VS-1000H mixed in ECM matrix to prevent emulsions from settling in the capillaries. The T_1 and T_2 of the major ^{19}F resonance were measured to be 570 and 182 ms, respectively. For sequence optimization, arraying of TR and TE resulted in clearly delineated contour lines produced by the interaction of both variables (Supplementary Fig. 3). Optimal parameters were defined as the central value of the contour line with the highest SNR for FLASH (TR = 1500 ms; TE = 5 ms), MSME (TR = 1500 ms; TE = 10 ms) and RARE (TR = 2500 ms; TE = 20 ms). TE was not arrayed for ZTE and FISP. Receiver bandwidth and flip angle also influences SNR (Fig. 2). Decreasing the receiver bandwidth increases SNR, but a too narrow bandwidth can increase chemical shift artifacts for PFC molecules with more than one major resonance peak. The interaction between TR and bandwidth defined optimal parameters for FLASH (18 kHz), MSME (20 kHz), RARE (20 kHz), ZTE (75 kHz) and FISP (30 kHz). Flip angle defines the optimal excitation of the ^{19}F spins to produce a maximum signal intensity. An array of flip angles against TR revealed optimal parameters for FLASH (90°), MSME (90°), RARE (90°), ZTE (3.5°) and FISP (60°). These values correspond closely to the theoretical optima. Table 2 summarizes optimal sequence parameters. These optimal parameters were used for all subsequent comparisons.

3.3. Optimized FISP sequence produced highest SNR

FISP achieved the highest SNR of 217 for a 100 mM PFPE nanoemulsion, with RARE yielding a 3.2× lower SNR (Fig. 3A). MSME produced an SNR almost 10× lower than FISP. The FISP sequence, however, produced 4.5× more noise than RARE, but the signal intensity for FISP was 15× higher than RARE. The SNR rank order of sequences was 1) FISP, 2) RARE, 3) FLASH, 4) ZTE, 5) MSME. To illustrate the use of these optimized sequences for the detection of infiltrating PFC-labeled macrophages, we imaged *ex vivo* a rat brain with implanted ECM hydrogel following experimental stroke (Fig. 3B). High noise levels and low ^{19}F signal intensity were evident in the ECM hydrogel in the stroke cavity, as well as in the scalp wound in the MSME, ZTE and FLASH images. A poor detection and localization of the invading macrophages is achieved in these scans. A robust signal in both the skull incision wound and the ECM is evident in the RARE and FISP images. However, the definition of the ^{19}F signal and its localization at the edge of the lesion cavity in the FISP scan provided a clearer picture of PFC-labeled macrophage trafficking than in the RARE scans, which contained more noise artifacts.

Table 1
Parameter arrays for optimization of sequence.

Sequence	TR (ms)	TE (ms)	Bandwidth (kHz)	Flip angle (°)
FLASH	100, 500, 1000, 2000	5, 10, 20	10, 20, 40, 60	40, 50, 60, 70, 80, 90
MSME	100, 500, 1000, 2000	5, 10, 20, 40	10, 20, 40, 60	40, 50, 60, 70, 80, 90
RARE	500, 1000, 2000, 2500	15, 30, 45, 60	10, 20, 40, 60	40, 50, 60, 70, 80, 90
ZTE	3.2, 3.4, 3.6, 3.8, 4		40, 75, 110	1, 2, 3, 4
FISP	3.8, 4, 6, 8		15, 20, 30, 40, 50	30, 40, 50, 60, 70, 80, 90

3.4. Signal averaging is required to improve detection and reduce noise

Number of averages (*NA*) or excitations is the number of times the time-domain data is repeatedly acquired and summed to maximize signal acquisition and reduce noise, with SNR gain proportional to $\sqrt{NA}$. For all optimized sequences increasing the signal averaging or scan time from 15 to 120 min (8×) increased the SNR by at least 2.5 times, which is close to the 2.8× increase that can be expected based on theoretical calculations (Supplementary Fig. 4A). At high concentrations (>20 mM), the ^{19}F signal was detectable (SNR >3) for all sequences using only NA = 1 (0.5 sec-2.5 min scan time). Contour plots further highlight the interaction between PFC concentration and scan time for the different sequences (Fig. 4A). Especially for the FISP sequence, it is evident that a greater range of signal is acquired for different PFC concentrations, with a 60 min scan being sufficient to contrast these. A comparison of sequences revealed FISP achieving the highest SNR for all PFC concentrations, followed by RARE and FLASH sequences (Fig. 4B). In order of sensitivity, the detection threshold at an SNR of 2 defined the limit of detection for FISP at 0.43 mM, RARE at 2.85 mM, FLASH at 3.84 mM, MSME at 5.46 mM, and ZTE at 3.77 mM at a 96 × 96 matrix size (Table 3). These concentrations are reported as mM of PFPE, multiplication by 42 yields the ^{19}F atom concentration. The effect of signal averaging on the *ex vivo* head sample was also determined by arraying scan times (0.5 sec–120 min) for each sequence (Fig. 4C). FISP and RARE achieved a more robust localization of PFC-labeled macrophages, while FLASH, MSME and ZTE showed poor localization and SNR inside the brain tissue, as well as the scalp incision. A 30 min scan was too short to afford a robust visualization of macrophage activity in the ECM hydrogel for all scans, although FISP detected areas with a high ^{19}F signal, while missing areas with a weaker signal (Type II error).

3.5. Smaller voxel sizes improve localization of ^{19}F signal

Image matrix size defines the information resolution, whereas the voxel size determines spatial resolution. By maintaining the same field-of-view, increasing matrix size improves both information and spatial resolution given high enough SNR. Although a small matrix and large voxel size achieves a higher SNR, partial volume effects (e.g. signal spill-over) are increased and it is difficult to localize the ^{19}F signal to specific neuroanatomical structures. Matrix/voxel size affected ^{19}F detection more in sequences achieving a low SNR, such as FLASH and MSME (Supplementary Fig. 4B). For instance, to achieve the same SNR a concentration greater than 5× was required by increasing matrix size from 32 × 32 (1.25 × 1.25 mm in-plane resolution) to 128 × 128 (0.31 × 0.31 mm in-plane resolution) using the FLASH sequence. RARE exhibited a more attenuated effect of matrix size (i.e. contour lines are flatter), with SNR being more dependent on PFC concentration (Fig. 5A). Th SNR of the FISP sequence was very consistent across the matrix sizes

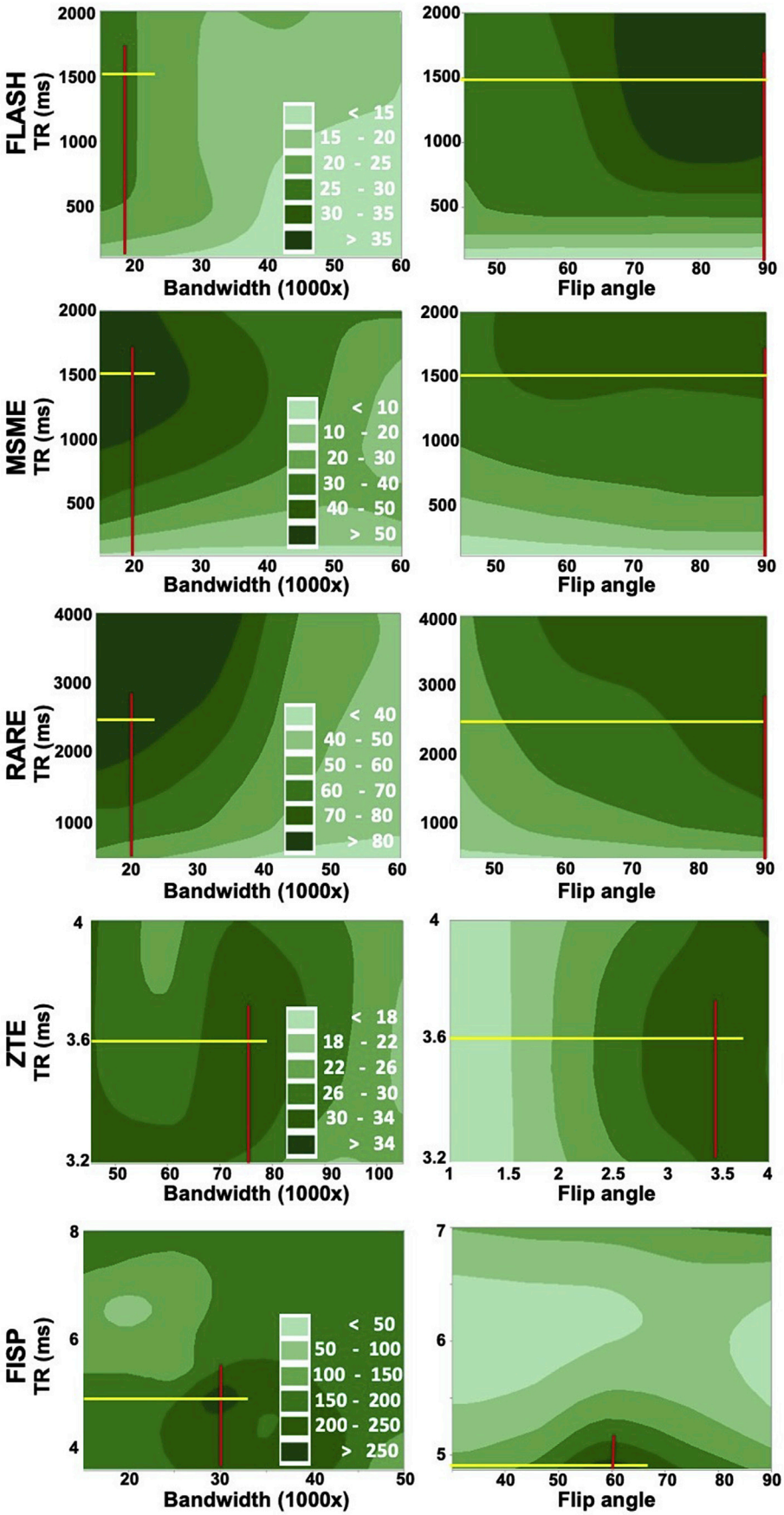

Fig. 2. Optimization of sequence parameters. To determine the optimal sequence parameters for PFC detection, these were arrayed from a low to a high value for repetition time (TR), Bandwidth, and flip angle. SNR was calculated for each scan and contour plots were computed to highlight the interaction between these independent variables. The optimal parameters for each imaging sequence were defined by the central value (yellow and red lines) of the contour line that yielded the highest SNR.

Table 2
Optimal acquisition parameters (n.a. = not applicable).

Sequence	TR (ms)	TE (ms)	Bandwidth (kHz)	Flip angle (°)
FLASH	1500	5	18	90
MSME	1500	10	20	90
RARE	2500	20	20	90
ZTE	3.6	n.a.	75	3.5
FISP	4.8	2.4	30	60

tested for low ^{19}F concentrations (<40 mM), but SNR was reduced at a concentration >60 mM when matrix size is increased (i.e. reducing voxel size). A comparison of sequences using a 96 × 96 matrix size (0.42 mm in-plane resolution) revealed that FISP achieved the highest SNR for all concentrations, followed by RARE and FLASH sequences (Fig. 5B). As imaging is a compromise to achieve sufficient SNR, as well as spatial information to localize the signal, an optimal matrix/voxel size is a trade-off between these two parameters.

To illustrate the effect of these on the ^{19}F detection of PFC-labeled macrophages, an *ex vivo* head using different matrix sizes with a fixed FOV was acquired to compare the efficiency of the sequences. Smaller matrix sizes revealed a strong ^{19}F signal, but compared to large matrix sizes indicated spill-over effects that produced a "hot spot" area that is larger than seen with greater resolution (Fig. 5C). Conversely, a 128 × 128 matrix size resulted in a lower ^{19}F signal and increased background noise, especially in the FLASH, MSME and ZTE sequences. The RARE sequence produced a high ^{19}F signal, with a low level of noise at the 96 × 96 matrix size, but noise and signal loss compromised detection at the 128 × 128 matrix size. FISP exhibited minimal noise at the 128 × 128 resolution, but some ^{19}F signal in the ECM-filled cavity was difficult to detect. A 96 × 96 matrix size using the FISP sequence produced the best compromise between SNR and being able to spatially localize the ^{19}F signal to anatomical structures.

3.6. FISP affords use of thinner image slices

As matrix size defines the spatial information covered in-plane, slice thickness and number of slices define coverage of anatomy in the caudal-rostral direction in supine rodents. Increasing slice thickness expands voxel size, which is often used to boost sensitivity. As expected, for the PFC phantoms, a slice thickness of 2 mm produced the highest SNR for all sequences and there was a proportional decline of SNR with thinner slices of 1.5 and 1 mm (Supplementary Fig. 4C). There was little interaction between changes in PFC concentration and slice thickness with concentration being the main determinant of SNR (Fig. 6A). The high sensitivity of the FISP sequence was advantageous in reducing slice thickness. A 1 mm slice using the FISP sequence produced a higher SNR than a 2 mm slice thickness for FLASH, MSME or ZTE. The SNR of the RARE sequence at 1.5 mm slice thickness was almost equivalent to the 1 mm slice SNR for the FISP. FISP achieved the highest SNR for a 1.5 mm slice, being 1.2× RARE, 2.4× FLASH, 2.8× MSME and 4.2× ZTE sequences (Fig. 6B). *Ex vivo* ^{19}F brain scans further indicated that thinner slices contained less signal than thicker slices (Fig. 6C). For FLASH and ZTE sequences, even with thick slices (2 mm = 4.76× the in-plane resolution) did not afford a robust detection of the incision wound on top of the head or macrophages invading ECM in the stroke lesion. MSME provided a localization, but a 1 mm slice also poorly delineated the presence of PFC-labeled macrophages in relation to anatomy. In contrast, RARE and FISP both provide a detailed view of macrophage distribution inside the ECM hydrogel even at 1.5 mm thickness (3.57× the in-plane resolution). The thinner slices provided a better graduation of the ^{19}F signal compared to the thicker slices, where edges exhibited a disproportionally strong signal compared to macrophages in the material. Although 1 mm slices (2.38× the in-plane resolution) are even better to define anatomy in the slice (i.e. z) direction, insufficient signal is visualized to afford a robust attribution to different anatomical structures.

3.7. Increasing matrix size improves accuracy of hot spot sizing and separation

Hot spot size and separation are major determinants of partial volume effects that can compromise the localization of macrophages to anatomical regions. To quantify the accuracy of object identification, as well as separation, point spread functions (PSFs) were acquired for hot

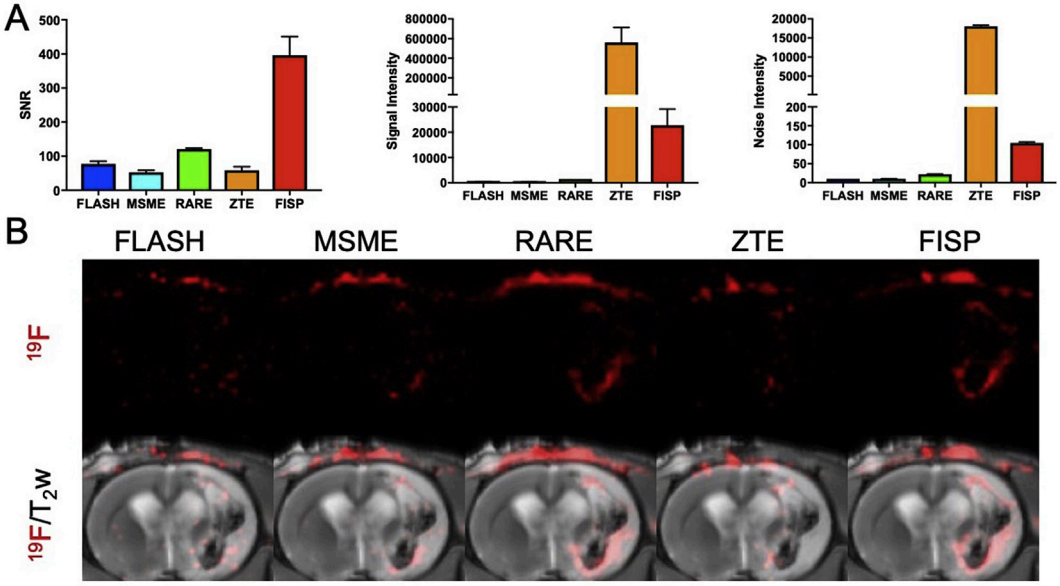

Fig. 3. Comparison of detection sensitivity. A. Using optimized imaging sequences, ^{19}F SNR was measured on a 100 mM PFC nanoemulsions with 20 min of scanning to afford a comparison of detection sensitivity. FISP achieved the highest SNR, followed by the RARE and FLASH sequences. ZTE produced the highest signal, but also the highest level of noise. **B.** The influence of noise on signal detection is especially apparent in the head phantom. The FISP sequence provides the most robust visualization of PFC-labeled macrophages against background. ECM invading macrophages can be clearly delineated on the FISP and RARE sequence, but the other sequences are insufficient to reliably detect and localize macrophage invasion in the brain. However, the peripheral accumulation of PFC-labeled macrophage in the scalp incision wound can also be seen using the MSME sequence.

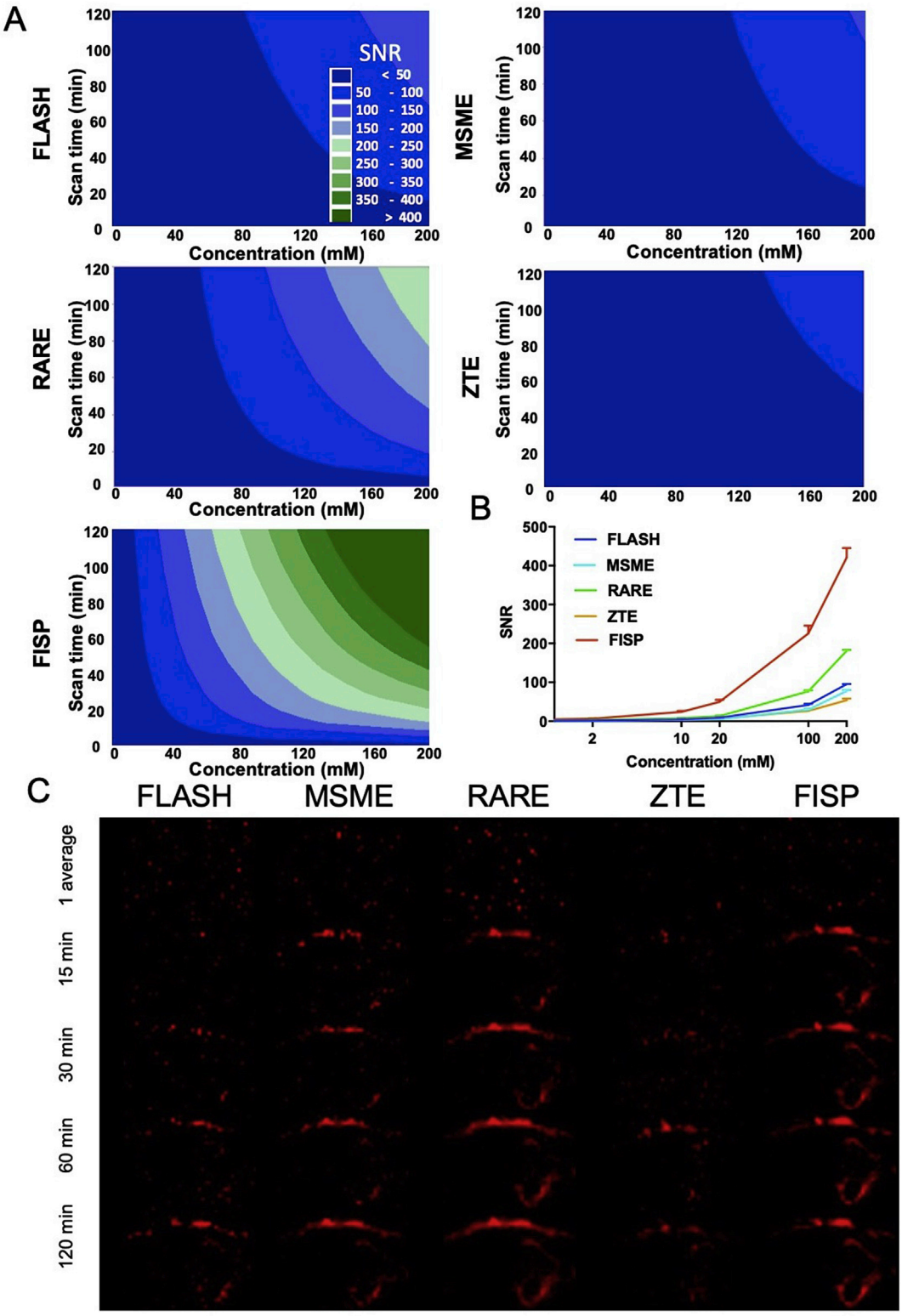

Fig. 4. **^{19}F signal per time unit. A.** To determine the effects of signal averaging on SNR, scanning time was arrayed (0.5 s–120 min) to provide a direct comparison of SNR for the different sequences using the same unit of time. Increasing the scan times improved the SNR for all sequences and concentrations. FISP consistently outperformed other sequences per unit time, followed by RARE. **B.** A comparison of optimized sequences for 60 min scan time indicated FISP achieving the highest SNR for all concentrations, followed by RARE and FLASH. **C.** *Ex vivo* ^{19}F imaging of a head phantom (96 × 96 matrix, 1.5 mm slice thickness) further illustrated the importance of signal averaging to reduce noise and differentiate the PFC signal. FISP is the most efficient sequence in reducing noise and maximizing the detection of PFC.

Table 3
Limits of detection (LOD). LOD at a SNR (y) = 2 detection was threshold determined by linear regression. The limit of detection concentration (x) for PFPE (VS1000) in mM was determined by (y - b)/m, where b is the intersect and m is the slope. To convert PFPE concentration into ^{19}F atom concentration, multiply LOD by 42. *LOD for the 32 × 32 FISP experiment was not determined (n.d.) because of spill-over image artifacts compared to other sequence using the same parameters.

Sequence	32 × 32 (3.12 mm^3)	64 × 64 (0.78 mm^3)	96 × 96 (0.35 mm^3)	128 × 128 (0.2 mm^3)
FLASH	(y-1.90)/0.931 = 0.107 mM	(y-0.766)/0.543 = 2.27 mM	(y-0.527)/0.382 = 3.85 mM	(y-0.769)/0.263 = 4.66 mM
MSME	(y-0.825)/0.755 = 1.55 mM	(y-0.094)/0.421 = 4.52 mM	(y-0.521)/0.270 = 5.47 mM	(y-0.568)/0.177 = 8.1 mM
RARE	(y-0.273)/1.31 = 1.31 mM	(y-0.192)/0.928 = 1.94 mM	(y-0.143)/0.651 = 2.85 mM	(y-0.259)/0.496 = 3.51 mM
ZTE	(y-1.17)/0.474 = 1.75 mM	(y-0.636)/0.551 = 2.47 mM	(y-0.865)/0.300 = 3.78 mM	(y-0.672)/0.203 = 6.52 mM
FISP	n.d.*	(y-1.80)/3.00 = 0.067 mM	(y-0.916)/2.49 = 0.43 mM	(y-1.02)/1.48 = 0.65 mM

spots measuring 1.8, 0.9 and 0.4 mm at 1.5, 1, and 0.5 mm apart (Supplementary Fig. 5). Matrix size was further arrayed (32 × 32, 64 × 64, 96 × 96 and 128 × 128 for in-plane resolutions of 1.25 mm 0.62 mm, 0.42 mm, 0.2 mm, respectively) to determine how voxel size influences the identification of individual hot spots. PSFs were compared to the actual physical measurements of hot spots to define the full width half maximum (FWHM), which was used to calculate the absolute error of measurement (Supplementary Fig. 6). A 32 × 32 matrix size produced the highest level of errors for all sequences and measurements, up to twice (i.e. 3.6 mm) the size of the actual object. These were mainly spill-over effects, where object size on the MR was larger than the actual object. Almost all other conditions produced the opposite effect, where objects on the MR image were smaller than they actually were (i.e. partial volume loss). However, the magnitude of this effect was much smaller with error typically less than 1 mm. Smaller objects (0.4 mm in diameter) were more accurately detected, due to a reduction in partial volume effects. Overall, the higher the matrix (and the smaller the voxel size) the more accurate object measurements were. The pattern of error across sequences was fairly consistent, with a 32 × 32 matrix being adequate only for measurements of large objects separated by a large distance (Fig. 7). A matrix size of 96 × 96 (0.42 mm resolution) was sufficient to have a reduced error for small objects (0.4 mm) separated by a small distance (0.5 mm). Little additional benefit was observed using the 128 × 128 matrix (0.2 mm voxel size). This pattern was consistent across all sequences.

Accuracy of hot spot separation measurements at 50% signal intensity indicated that even small gaps of 0.5 mm could be distinguished with 1.8 mm objects with minimal error (Supplementary Fig. 7). For 1.8 mm sized objects, there was little difference between matrix sizes. However, for 0.9 and 0.4 mm objects, the 32 × 32 matrix underestimated gap size, especially with larger gaps. This is due to spill-over effects from hot spots. As expected, this effect was less pronounced with larger matrix sizes (i.e. smaller voxels). Gaps between smaller objects using matrix sizes larger than 32 × 32, typically overestimated gap size due to partial volume effects, in which voxels in the gap had insufficient signal to define the edge of the hot spot. The error for the 32 × 32 matrix was lowest using the ZTE sequence and highest for RARE. This pattern was fairly consistent for all sequences. Contour plots further support these differences and indicate that a matrix size of at least 64 × 64 matrix reduces partial volume effects that lead to an over- or under-estimation of gap size (Fig. 8). Little benefit in accuracy is observed with a 128 × 128 matrix size even for 0.4 mm objects at a distance of 0.5 mm. A 96 × 96 matrix therefore is sufficient for a hot spot separation at these dimensions. Appropriate estimation of gap size is important, as it could lead to an overestimation of the area affected by macrophage invasion and complicate the attribution of their location to a specific neuroanatomical substrate.

Partial volume effects determining hot spot separation can also affect image contrast, i.e. the magnitude of the noise (low signal in between hot spots) and signal measurement (peak measurement of hot spot). The small matrix size of 32 × 32 reduced contrast between hot spots indicating a spill-in of signal from hot spots (Supplementary Fig. 8). However, a 64 × 64 matrix size was sufficient to avert these effects for large objects of 1.8. mm, but with smaller objects a 64 × 64 matrix was insufficient. A 96 × 96 or higher matrix was needed to provide a high contrast between hot spots. The pattern of contrast between sequences was consistent, although the magnitude of contrast between sequences was their detection sensitivity. The consistency in contrast patterns between sequences was further evident in contour plots (Fig. 9). A high contrast was evident for large objects (1.8 mm) and a large gap (1.5 mm) with a large matrix size (i.e. small voxel size). As the gap decreases, a smaller smaller voxel size is required to define this gap more accurately, based on the magnitude of the contrast. As object size decreases, it is more difficult to achieve a high contrast with a small gap. At the 0.9 object size, contrast is affected by both a loss of signal (large gap size) and spill-over effect (small gap size), with a more optimal contrast at an intermediate gap size. In these measures, FLASH and MSME provided the highest contrast, whereas FISP provided the lowest contrast between hot spots. These differences potentially reflect the influence of the high signal produced by hot spots using the FISP sequence, which leads to greater partial volume effects between hot spots. These partial volume effects are less evident at the small object size, where contrast is predominantly determined by matrix/voxels size, with smaller voxels providing the best distinction between noise and signal. Analysis of hot spot separation illustrates the importance of object and voxel size to appropriately interpret ^{19}F images. Large voxel volumes carry a high risk of overestimating the distribution and number of macrophages that invaded ECM hydrogel. A 96 × 96 matrix (0.42 mm resolution) minimizes this risk, but even smaller voxel sizes would further improve the mapping of macrophage hot spots.

4. Discussion

The spatio-temporal mapping of macrophage invasion into ECM hydrogel through host brain tissue requires an efficient acquisition strategy. This needs to reconcile a high spatial resolution, while achieving sufficient signal, as well as contrast, to localize and distinguish regional macrophage activity. We here optimized commonly used ^{19}F MR imaging sequences for an SNR comparison to determine the most efficient acquisition strategy. FISP and RARE achieved the highest ^{19}F signal per time unit. Detection thresholds of 0.43 mM (18.1 mM ^{19}F atom concentration) for FISP and 2.85 mM (120 mM ^{19}F atom concentration) for RARE were achieved with a 96 × 96 matrix (0.42 mm in-plane resolution, 2 mm slice thickness) in 60 min scan time. A robust delineation of macrophage hot spots was evident with a slice thickness of 1.5 mm (3.57× the in-plane resolution). This matrix size and resolution was also sufficient to reduce partial volume effects to afford the reliable identification and separation (0.5 mm) of smaller hot spots (0.4 mm). Although these parameters are adequate for macrophage mapping within a 60 min scan time, further improvements are desirable to detect smaller clusters of cells, while minimizing partial volume effects.

4.1. ^{19}F acquisition efficiency improves PFC detection

The limit of detection (LOD) for PFC is defined by the detection threshold. The detection threshold is set at a value where signal can be accurately and reliably distinguished from background noise (Smith, 1997). As ^{19}F molecules are not naturally abundant in air or in organic tissue (i.e. physiological noise), the noise component in ^{19}F MR images is

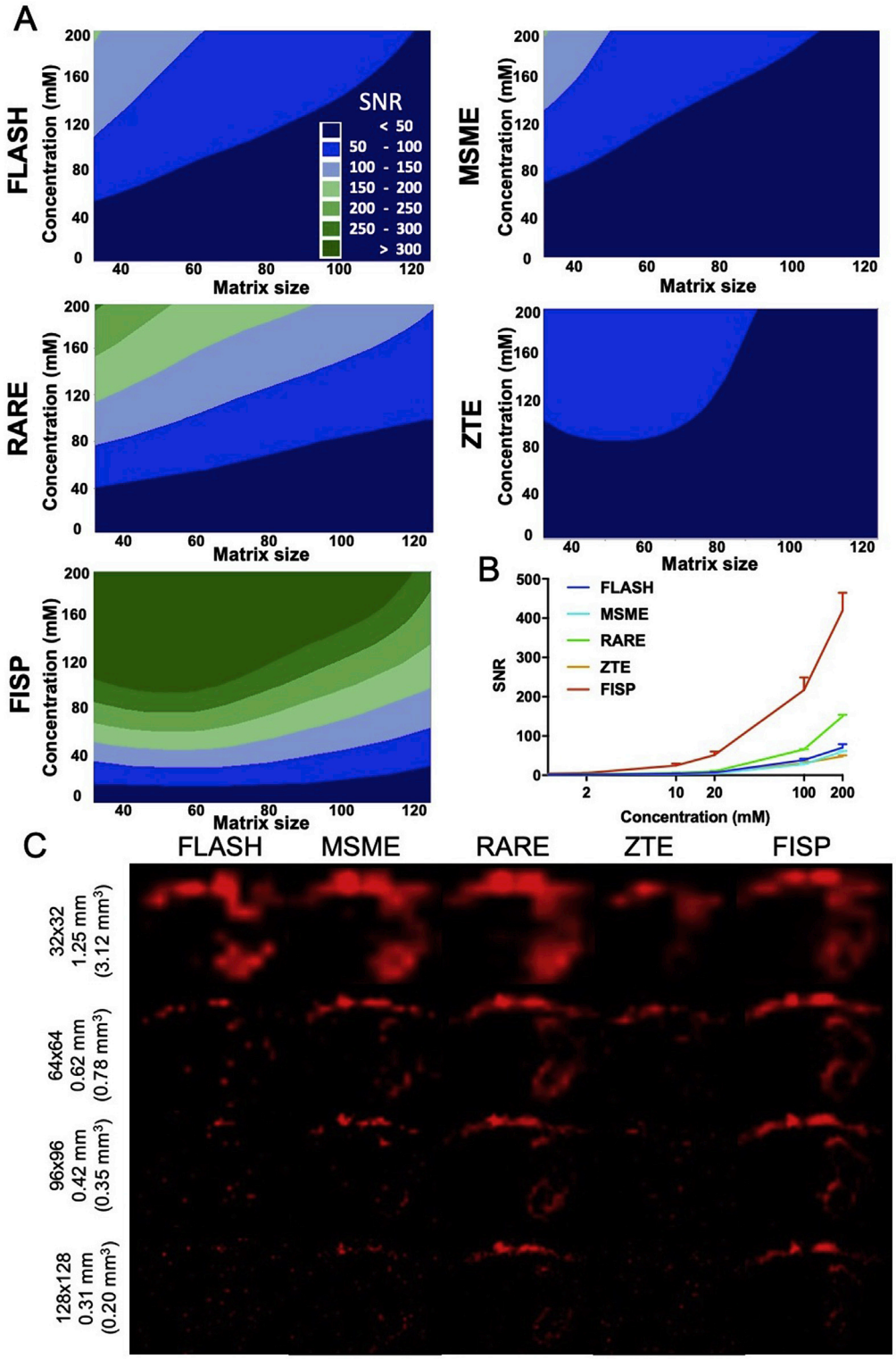

Fig. 5. Reducing partial volume effects based on voxel volume. A. To determine the interaction between PFC concentration and matrix size (128 × 128, 96 × 96, 64 × 64, 32 × 32), SNR was measured for each sequence (20 min scans) to compute contour plots. Higher concentrations and larger voxel sizes (i.e. smaller matrix size) increased SNR. Increases for the FLASH, MSME and RARE sequences were almost linear, but this was not the case for ZTE and FISP. FISP provided the greatest gradation of SNR across PFC concentrations, especially lower doses. **B.** A comparison of optimized sequences using 96 × 96 matrix (0.35 mm^3) indicated that FISP achieved the highest SNR across all sequences and concentrations. **C.** ^{19}F *ex vivo* images of a head phantom further support these differences with FISP providing the more defined signal localization with minimal background noise. However, scans with larger voxel sizes (i.e. smaller matrix size) revealed spill-in and -over effects in neighboring voxels. This produces the appearance of a larger area being covered by macrophage than is evident on scans with smaller voxels. A 96 × 96 matrix size (0.35 mm^3 voxel volume) here provided an adequate distinction and localization of ^{19}F signal using the FISP sequence. RARE also provided some definition of the ^{19}F signal, but was less precise using a 96 × 96 matrix size compared to FISP. Using a 128 × 128 matrix size, SNR was reduced and affected the discrimination of the PFC against background.

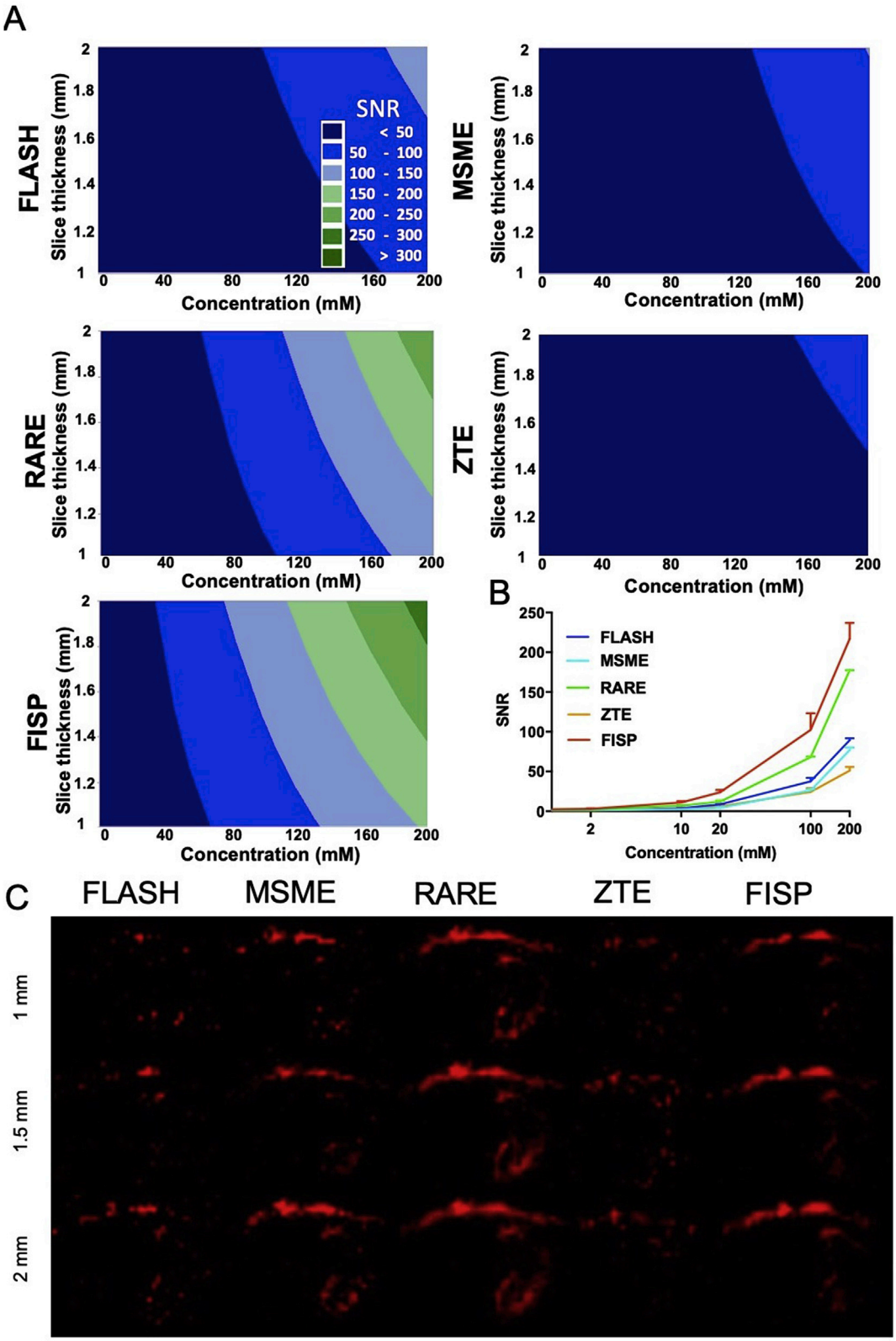

Fig. 6. Partial volume effects and slice thickness. To determine the effect of slice thickness on ^{19}F SNR, scans were acquired with 1, 1.5, and 2 mm slice thicknesses. **A.** Increasing slice thickness improves SNR for all sequences, with FISP achieving the highest SNR for all ^{19}F concentrations. **B.** A comparison of optimized sequences with 1.5 mm slice thickness (96 × 96 matrix; 60 min acquisition time) achieved the highest SNR for FISP, followed by RARE and FLASH. **C.** An *ex vivo* scan with different slice thicknesses illustrated the more precise localization (i.e. less blurring and hot spot signal saturation) with decreasing slice thicknesses.

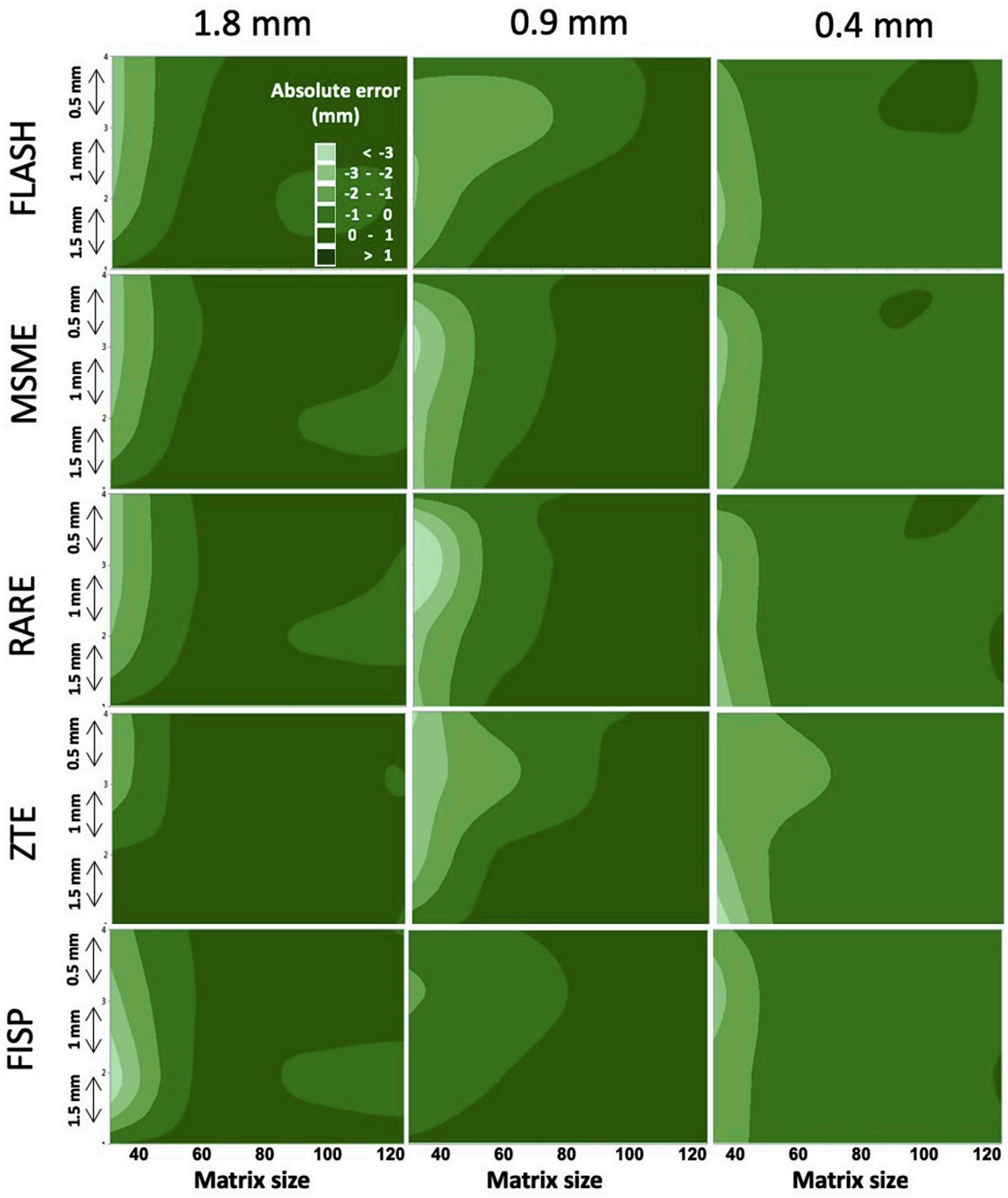

Fig. 7. Defining the accuracy of the hot spot signal. To define the accuracy of ^{19}F acquisition, the full width at half maximum (FWHM) was measured at $I_{max}/2$. The absolute error was calculated based on the known physical and measured size of each object. Smaller voxels with a larger matrix size (128 × 128) achieved the most accurate definition of objects, whereas 32 × 32 was the least accurate. As the distance in between objects increased, the accuracy of the PSF improved.

primarily thermal (Johnson-Nyquist) noise produced by electrical circuits in the coil and follows a Rician distribution (Gudbjartsson and Patz, 1995). Due to the lack of a normal distribution, the use of the standard deviation of noise as a divisor is inappropriate for SNR calculations. A scaling factor cannot appropriately correct for the nature of noise distribution and the large disparity in voxels containing signal (<3%) versus noise (65%), which affects the Kurtosis of the distribution curves. A negative control sample (i.e. no ^{19}F signal present) should not produce an SNR ($\overline{S}/\overline{N}$) that is higher than 1 (i.e. noise divided by noise). Dividing mean signal by mean noise hence calculates an easily interpretable SNR. We demonstrate here that there is some overlap in the intensity distribution between the noise and ^{19}F signal that can lead to type I and II errors. The intersection point between both distributions was at 52% above the mean of the noise intensity, indicating that thresholds of 25% or 1 standard deviation (37%) above mean noise are inappropriate as detection thresholds. An SNR of 2 here defined a conservative detection threshold that included <1% of noise, but harbors the risk that some voxels (16.7%) with very low concentrations of PFC are not identified as signal (type II error).

Although the detection threshold defines the separation of signal from noise, the limit of PFC detection is also influenced by voxel size and image averaging. To provide a comparison between sequences and voxel size, all samples were acquired using the same imaging parameters. LOD for FLASH, MSME and ZTE decreased with smaller voxel sizes. These

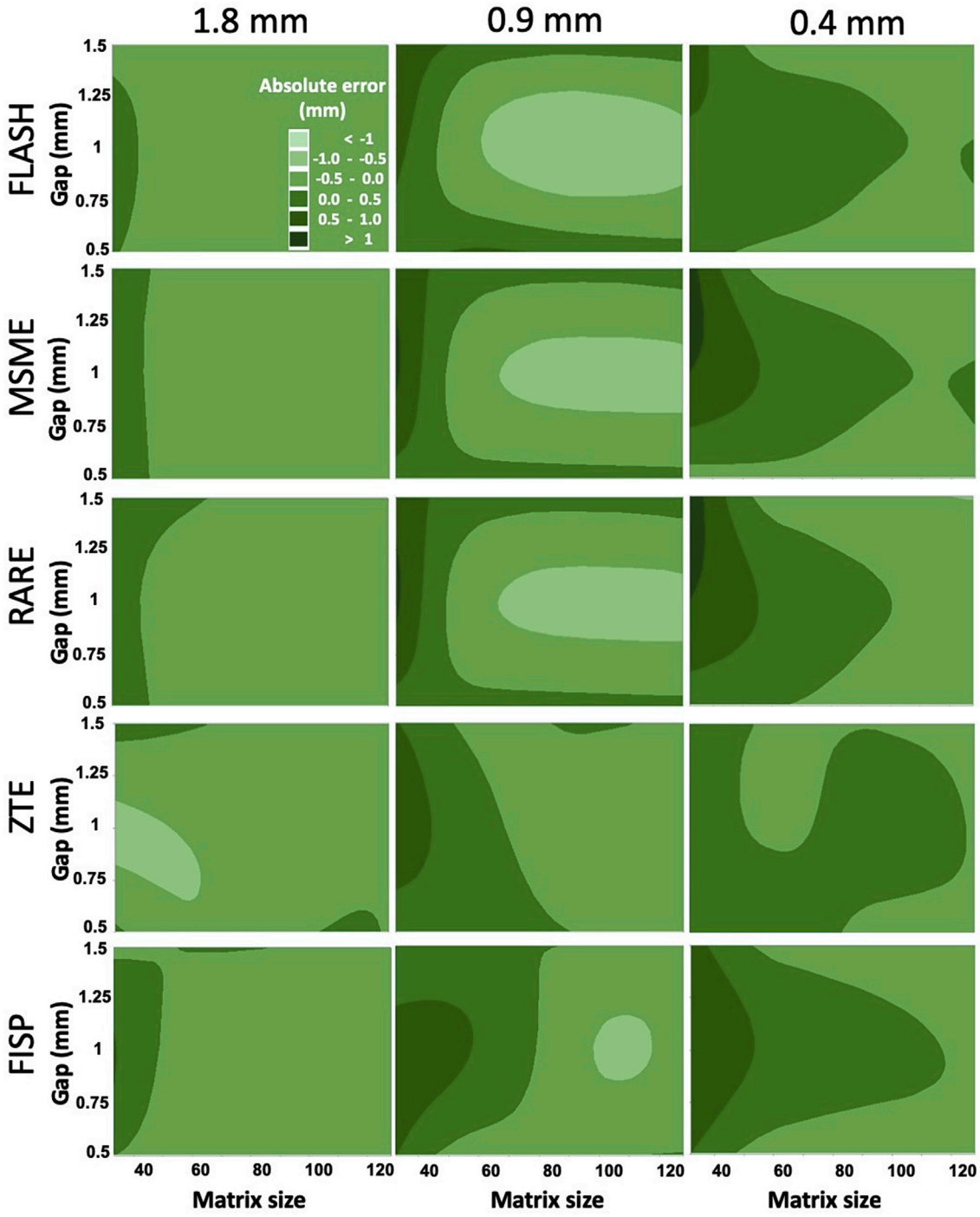

Fig. 8. Defining distance between hot spots. Separation distance between two PSFs was measured at 50% I_{max}. A bigger matrix size reduced measurement error of the distance between all objects, but was more important to distinguish smaller objects. Medium sized objects were most accurately distinguished at a distance (1 mm) that was equivalent to the object. Smaller voxel sizes produced partial volume effects that increased error measurements.

sequences were less efficient at detecting PFC compared to the FISP and RARE sequences, producing overall lower SNR in direct comparisons. At 9.4T, the 96×96 matrix size with a 2 mm slice thickness (0.35 mm^3 voxel) produced a LOD for a 60 min RARE of 2.85 mM (120 mM ^{19}F atoms) and FISP of 0.43 mM (18.1 mM ^{19}F atoms). These estimations were verified experimentally by lower concentration samples that failed to reach an SNR >2. Spatial resolution is therefore a major factor in achieving an optimal imaging outcome with larger voxels not always producing the highest LOD, mostly due to partial volume effects. The LOD for RARE (Turbo Spin Echo) and FISP (Balance Steady-State Precession) was previously estimated to be 40.8 mM and 23.5 mM ^{19}F atoms for PFPE, with the computed sensitivity normalized to a 1 mm^3 voxel and 10 min of scanning using a 3T scanner (Colotti et al., 2017). Others have reported LODs for potassium hexafluorophospate at 0.5 mM (Mastropietro et al., 2014) and trifluoroacetic acid (TFA) at 0.948 mM (Taylor et al., 2016), but differences in compounds, field strength and methodology make comparisons with our results challenging. Our investigation here directly compared commonly used sequences and imaging

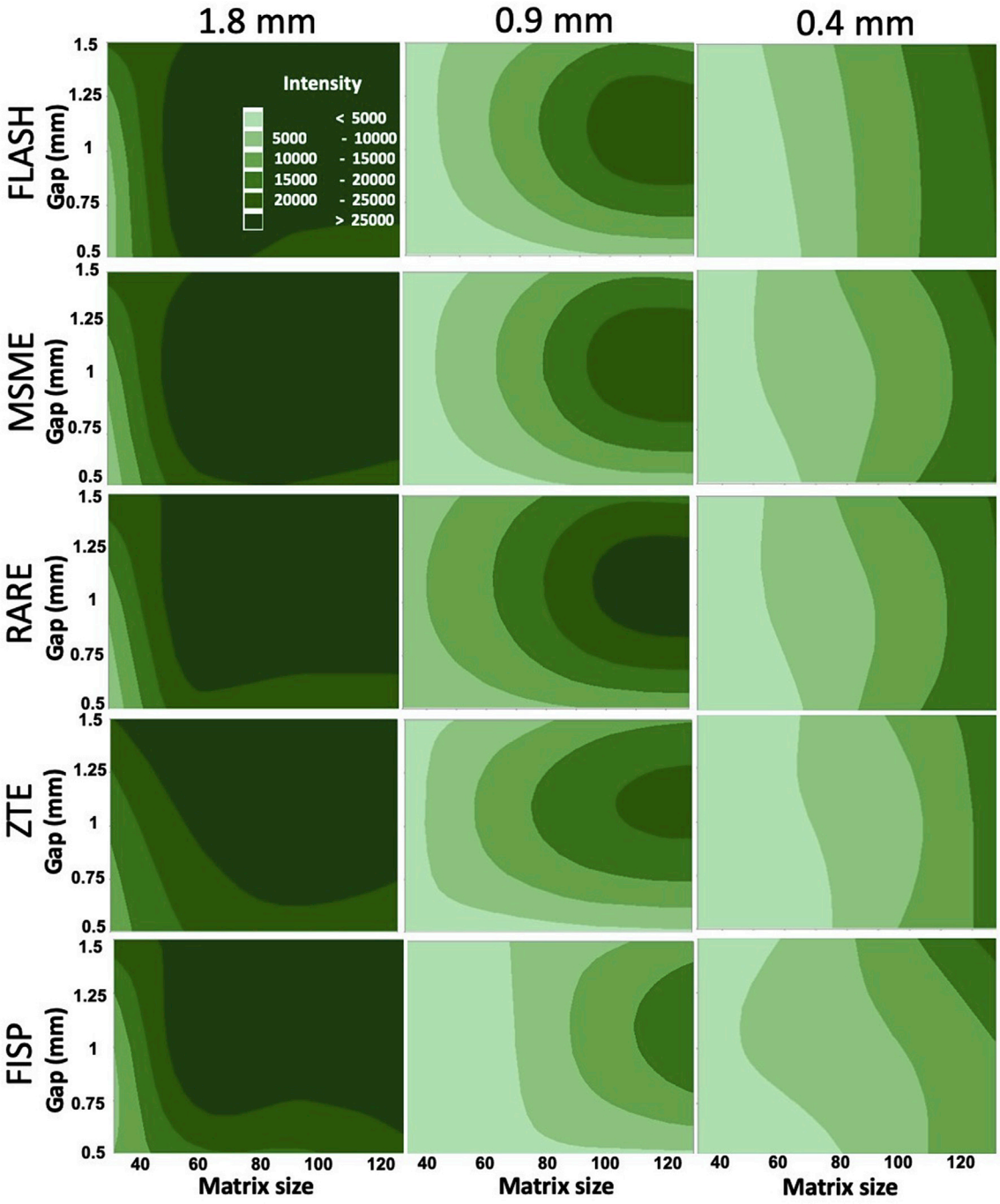

Fig. 9. Defining contrast to separate hot spots. The magnitude of signal separating the I_{max} from noise between two PSFs defines contrast. Larger voxels (32 × 32 matrix) here produced less contrast compared to smaller voxels (128 × 128 matrix). Larger objects, as well as a larger distance between these, further improved contrast. However, FISP was adept at distinguishing small capillaries of 0.4 mm size with a 0.5 mm gap between these using a 64 × 64 matrix size.

parameters to indicate that the FISP and RARE sequences are the most efficient sequences to acquire a PFC signal. FISP is favorable for a small number of slices, as the total acquisition time increases with number of slices. However, FISP is prone to banding and chemical shift artifacts (Nitz, 2002). RARE may be favorable for a greater number of slices, as multiple slices are acquired during TR. Optimized FISP conditions described here can acquire at least 14 slices before an increase in acquisition time is required to add further slices.

Although FISP and RARE are the most efficient sequences to acquire a ^{19}F signal, improvements in acquisition are desirable to further reduce the LOD and spatial resolution. Implementation of compressed sensing (Liang et al., 2017; Zhong et al., 2013a), signal deconvolution (Meissner et al., 2015) and advanced RF coil designs, including cryocoils to reduce thermal noise (Waiczies et al., 2013, 2017), can further improve the acquisition efficiency. Modification of contrast agents for macrophage imaging, using, for instance, super-fluorination, could further boost signal per cell to achieve a better detection of macrophages (Tirotta et al., 2014). Although the addition of paramagnetic agents can improve the detection efficiency of the fluorine signal (Chalmers et al., 2011; Gaudet et al., 2017; Hitchens et al., 2015; Jahromi et al., 2018; Kislukhin et al., 2016; Lee et al., 1994; Schmid et al., 2013), it remains unclear if these metals chelates will influence the detection of anatomy and pathology

using ^{1}H MR imaging, potentially compromising localization of the macrophages to a particular post-stroke microenvironment. We here optimized sequences for spin-density ^{19}F imaging, but combined imaging with metal chelates will require further adjustments to imaging parameters.

4.2. Identification and separation of hot spots is determined by imaging parameters

Beyond detecting a signal, key questions that arise in imaging are how small of an object or cluster of cells can be detected and separated from neighboring objects. Accuracy of these measurement is defined by its trueness (i.e. similarity of measured size to actual dimensions) and precision (i.e. consistency between multiple independent measurements) (ISO, 1994). These issues have mostly been ignored in ^{19}F-MR imaging (Keupp et al., 2011; Meissner et al., 2015), but are well defined issues in other hot spot imaging techniques, such as PET (Hoffman et al., 1979; Kessler et al., 1984) and SPECT (Beekman et al., 1999). Measurement of the PSF defines the trueness of measurements in the spatial domain to define signal intensities in voxels occupied by the object (Rahmim et al., 2013). Precision is defined by the differences in multiple independent measurements. Based on the PSF of individual hot spots, FWHM can be calculated (Markevich and Gertner, 1989) to afford an assessment of imaging accuracy based on known physical characteristics of hot spots, as well as their separation.

The axial PSF indicated that a matrix size of at least 64×64 (0.62 mm in-plane resolution) was required to accurately identify and separate objects of medium or small size. A 32×32 matrix size was largely inadequate to accurately identify and separate objects. However, also a 128×128 matrix size exhibited partial volume effects that were not evident with the 96×96 matrix size. This is likely a reflection of the size of objects used here with the smallest object (0.4 mm in diameter) being $1.3\times$ larger than its voxel size (0.31 mm). A 96×96 matrix size (0.42 mm resolution) here provided the most robust and reproducible (i.e. accurate) identification and separation of objects. This is double the in-plane voxel size (0.208 mm) of T_2-weighted images used to visualize the stroke cavity. Imaging parameters were the main determinants of partial volume effects and accuracy of object identification and separation. The effect of imaging sequences was mostly mediated through SNR which limited contrast. A fine balance is required to achieve sufficient signal (and contrast) to achieve the identification of an object. If the signal is too low, it results in partial volume loss, whereas a high signal produces a spill-over effect that leads to an overestimation of object size and an underestimation of object separation.

The matrix size defines digitization and in-plane resolution, but slice thickness defines voxel depth and the lateral PSF. Although ideally voxel size is isotropic, in low SNR imaging techniques this could lead to a poor in-plane resolution or insufficient SNR and contrast to interpret images. Unfortunately, a loss of contrast with higher resolution images cannot be regained by averaging to a lower resolution image through nearest neighbor, even though SNR is increased (Constable and Henkelman, 1991). Slice thickness is therefore often used to boost signal per voxel in a low signal regime. This is only effective if spin density carries through the slices, which can lead to issues in localizing and separating objects in the slice direction, especially if slice thickness is disproportionate to the in-plane resolution (Ogura et al., 2005). In ^{19}F imaging of rodent models, a slice thickness of 2 mm or larger is common. A 2 mm slice here produced a robust signal, but is $5.7\times$ the in-plane resolution of a 96×96 matrix and $1.6\times$ the resolution of a 32×32 matrix. A 1.5 mm slice thickness produced a compromise between slice thickness and signal on brain images, but is still $3.75\times$ the dimension of the 96×96 matrix. Based on the PSF measurement, this voxel depth is insufficient to resolve neighboring objects of a medium size. Considering partial volume effects is therefore essential to appropriately interpret hot spot images in their anatomical context (Alavi et al., 2018). In some cases, thinner slices with a gap are more favorable to detect and localize a signal than thick slices that are prone to partial volume effects and poorly align with the anatomical reality (Bradley and Glenn, 1987). Commonly in anatomical MR imaging, slice thickness is 2–3x the in-plane resolution, ideally this factor is maintained in ^{19}F imaging. Typical MR imaging in preclinical models of stroke uses a slice thickness of 0.5 mm (Ashioti et al., 2007; Ghuman et al., 2017; Stille et al., 2013). However, the ^{19}F signal in the 1 mm slice thickness here was lower than for 1.5 mm, with some hot spots being difficult to discern in the brain phantom. To ensure an appropriate contextualization and interpretation of ^{19}F hot spot images, anatomical scans might hence provide guidance to imaging parameters by adjusting matrix size and slice thickness by a factor of 2 to reduce partial volume effects in the axial and lateral directions and afford co-localization to brain microenvironments.

4.3. ^{19}F imaging for the mapping of macrophage invasion

PFC nanomelusions have been extensively used to visualize macrophage trafficking, but only a few studies have used this approach to investigate their role in neurological conditions (Flogel et al., 2008; Mastropietro et al., 2014; Temme et al., 2012; Waiczies et al., 2013; Zhong et al., 2013b, 2015). A major limitation is the smaller quantity of macrophages responding to brain lesions that typically occupy a smaller volume space. Mapping of macrophage invasion in the brain therefore requires a very efficient acquisition of the ^{19}F signal. Optimized FISP and RARE sequences here provided favorable conditions for PFC-labeled macrophage imaging in the brain. The importance of imaging parameters on partial volume effects was further demonstrated using a brain phantom. Based on these results, it can be stipulated that imaging of small areas will most efficiently be imaged using FISP, whereas the RARE sequence is advantageous to map macrophages distributed in a large area using thin slices. An acute time-course mapping of a small region with macrophage invasion is therefore best visualized using the FISP sequence, whereas the RARE sequence is more appropriate to map macrophage distribution and density across the whole brain. The ^{19}F imaging strategy therefore needs to be chosen in relation to the anatomical context of the lesion being monitored.

After stroke, different structural and physiological microenvironments develop that can be defined using MR imaging (Stille et al., 2013). Targeting of the lesion cavity for implantation of bioscaffolds requires a high resolution MR imaging-based guidance to ensure gelation and retention of the scaffold (Ghuman et al., 2016, 2017; Massensini et al., 2015). Macrophage invasion into the ECM bioscaffold is considered the pivotal mode of action to promote its biodegradation and facilitate the infiltration of host organ cells (Brown et al., 2014; LoPresti and Brown, 2018). Within 24 h > 150,000 macrophages invade ECM hydrogel implanted into a stroke cavity (Ghuman et al., 2016). A correlation of macrophage density with ECM hydrogel volume over 90 days indicated that their invasion, distribution and local density drive the biodegradation of the scaffold (Ghuman et al., 2018). At present, tedious histological time course studies are required to determine this distribution and density of macrophages in ECM hydrogel. However, macrophage invasion depends on the volume and topology of the cavity and the implanted scaffold, which vary considerably between subjects and complicate the comparison of different histological time points. Non-invasive mapping of macrophage invasion, distribution and density would provide an important complimentary technique to investigate the role of macrophages in tissue regeneration. PFC-labeled macrophages and their ^{19}F MR imaging could hence provide an important biomarker to monitor the process of bioscaffold degradation.

5. Conclusions

^{19}F MR imaging is an excellent tool for cellular imaging, as there are no physiological background signals caused by the presence of fluorine in the brain. The measured signal therefore is specific to the exogenous PFC nanoemulsions injected. Their uptake into macrophages through

phagocytosis offers a unique biomarker to visualize their participation in inflammatory events, such as the biodegradation of an ECM hydrogel. However, the relatively small number of ^{19}F atoms present in tissues limit the detection of invading labeled cells. Thus, this study compared imaging sequences and parameters. A comparison of optimized sequences here indicated that the FISP and RARE are the most efficient at acquiring the ^{19}F signal. However, imaging parameters also exert a major influence on the accuracy of measurements. Partial volume effects are evident with hot spot imaging and can compromise the interpretation of distribution and density of cells in tissue. An appropriate voxel resolution should be defined in relation to the anatomical context, typically imaged using ^{1}H MRI. Although thick slices are often used to improve signal, this compromises the localization of the ^{19}F signal to anatomical substrates. It is therefore recommended that ^{19}F imaging voxels are 2–3x the size of anatomical voxels in each direction. The systematic optimization of ^{19}F imaging detailed here afforded the visualization of PFC-labeled macrophages that invaded an ECM hydrogel implanted into a stroke cavity of a rat brain and hence provided an illustration of how these parameters affect detection in a potential application of this approach. The spatio-temporal mapping of the macrophage contribution to biodegradation in tissue regeneration could greatly improve our understanding of this process and facilitate its translation by providing a biomarker that affords monitoring of patients during clinical trials.

Authors contribution

HG conducted all experiments, created graphs, analyzed the data, contributed to the design of the study. TKH conceived of the study, contributed to the design of experiments and interpretation of the results. MM conceived of the study, oversaw experiments, contributed to the design of the experiments, interpreted results, provided funding and wrote the manuscript.

Acknowledgements

This work was partially supported by the National Institute of Neurological Disorders and Stroke (R01NS082226), the National Institute of Biomedical Imaging and Bioengineering (R01EB016629), and the Pennsylvania Department of Health (4100061184).

Appendix A. Supplementary data

Supplementary data to this article can be found online at https://doi.org/10.1016/j.neuroimage.2019.116090.

References

Ahrens, E.T., Bulte, J.W., 2013. Tracking immune cells in vivo using magnetic resonance imaging. Nat. Rev. Immunol. 13, 755–763.
Ahrens, E.T., Flores, R., Xu, H., Morel, P.A., 2005. In vivo imaging platform for tracking immunotherapeutic cells. Nat. Biotechnol. 23, 983–987.
Ahrens, E.T., Young, W.B., Xu, H., Pusateri, L.K., 2011. Rapid quantification of inflammation in tissue samples using perfluorocarbon emulsion and fluorine-19 nuclear magnetic resonance. Biotechniques 50, 229–234.
Ahrens, E.T., Zhong, J., 2013. In vivo MRI cell tracking using perfluorocarbon probes and fluorine-19 detection. NMR Biomed. 26, 860–871.
Alavi, A., Werner, T.J., Hoilund-Carlsen, P.F., Zaidi, H., 2018. Correction for partial volume effect is a must, not a luxury, to fully exploit the potential of quantitative PET imaging in clinical oncology. Mol. Imaging Biol. : MIB. Off. Publ. Acad. Mol. Imaging 20, 1–3.
Anisimov, N., Gulaev, M., Pavlova, O., Fomina, D., Glukhova, V., Batova, S., Prirogov, Y., 2017. Calculation of optimal parameters for 19F MRI. J. Phys. Conf. Ser. 886, 012001.
Ashioti, M., Beech, J.S., Lowe, A.S., Hesselink, M.B., Modo, M., Williams, S.C., 2007. Multi-modal characterisation of the neocortical clip model of focal cerebral ischaemia by MRI, behaviour and immunohistochemistry. Brain Res. 1145, 177–189.
Badylak, S., Arnoczky, S., Plouhar, P., Haut, R., Mendenhall, V., Clarke, R., Horvath, C., 1999. Naturally occurring extracellular matrix as a scaffold for musculoskeletal repair. Clin. Orthop. Relat. Res. S333–S343.
Badylak, S.F., 2004. Xenogeneic extracellular matrix as a scaffold for tissue reconstruction. Transpl. Immunol. 12, 367–377.
Badylak, S.F., Freytes, D.O., Gilbert, T.W., 2009. Extracellular matrix as a biological scaffold material: structure and function. Acta Biomater. 5, 1–13.
Beekman, F.J., Slijpen, E.T., de Jong, H.W., Viergever, M.A., 1999. Estimation of the depth-dependent component of the point spread function of SPECT. Med. Phys. 26, 2311–2322.
Bible, E., Chau, D.Y., Alexander, M.R., Price, J., Shakesheff, K.M., Modo, M., 2009. Attachment of stem cells to scaffold particles for intra-cerebral transplantation. Nat. Protoc. 4, 1440–1453.
Bible, E., Dell'Acqua, F., Solanky, B., Balducci, A., Crapo, P.M., Badylak, S.F., Ahrens, E.T., Modo, M., 2012. Non-invasive imaging of transplanted human neural stem cells and ECM scaffold remodeling in the stroke-damaged rat brain by (19)F- and diffusion-MRI. Biomaterials 33, 2858–2871.
Boehm-Sturm, P., Mengler, L., Wecker, S., Hoehn, M., Kallur, T., 2011. In vivo tracking of human neural stem cells with 19F magnetic resonance imaging. PLoS One 6 e29040.
Bonner, F., Merx, M.W., Klingel, K., Begovatz, P., Flogel, U., Sager, M., Temme, S., Jacoby, C., Salehi Ravesh, M., Grapentin, C., Schubert, R., Bunke, J., Roden, M., Kelm, M., Schrader, J., 2015. Monocyte imaging after myocardial infarction with 19F MRI at 3 T: a pilot study in explanted porcine hearts. Eur Heart J Cardiovasc Imaging 16, 612–620.
Bouchlaka, M.N., Ludwig, K.D., Gordon, J.W., Kutz, M.P., Bednarz, B.P., Fain, S.B., Capitini, C.M., 2016. (19)F-MRI for monitoring human NK cells in vivo. OncoImmunology 5 e1143996.
Bradley, W.G., Glenn, B.J., 1987. The effect of variation in slice thickness and interslice gap on MR lesion detection. AJNR Am J Neuroradiol 8, 1057–1062.
Brown, B.N., Sicari, B.M., Badylak, S.F., 2014. Rethinking regenerative medicine: a macrophage-centered approach. Front. Immunol. 5, 510.
Bulte, J.W., 2005. Hot spot MRI emerges from the background. Nat. Biotechnol. 23, 945–946.
Bulte, J.W., Frank, J.A., 2000. Imaging macrophage activity in the brain by using ultrasmall particles of iron oxide. AJNR Am J Neuroradiol 21, 1767–1768.
Chalmers, K.H., Kenwright, A.M., Parker, D., Blamire, A.M., 2011. 19F-lanthanide complexes with increased sensitivity for 19F-MRI: optimization of the MR acquisition. Magn. Reson. Med. 66, 931–936.
Colotti, R., Bastiaansen, J.A.M., Wilson, A., Flogel, U., Gonzales, C., Schwitter, J., Stuber, M., van Heeswijk, R.B., 2017. Characterization of perfluorocarbon relaxation times and their influence on the optimization of fluorine-19 MRI at 3 tesla. Magn. Reson. Med. 77, 2263–2271.
Constable, R.T., Henkelman, R.M., 1991. Contrast, resolution, and detectability in MR imaging. J. Comput. Assist. Tomogr. 15, 297–303.
Crapo, P.M., Gilbert, T.W., Badylak, S.F., 2011. An overview of tissue and whole organ decellularization processes. Biomaterials 32, 3233–3243.
Flogel, U., Ding, Z., Hardung, H., Jander, S., Reichmann, G., Jacoby, C., Schubert, R., Schrader, J., 2008. In vivo monitoring of inflammation after cardiac and cerebral ischemia by fluorine magnetic resonance imaging. Circulation 118, 140–148.
Gaudet, J.M., Hamilton, A.M., Chen, Y., Fox, M.S., Foster, P.J., 2017. Application of dual (19) F and iron cellular MRI agents to track the infiltration of immune cells to the site of a rejected stem cell transplant. Magn. Reson. Med. 78, 713–720.
Ghuman, H., Gerwig, M., Nicholls, F.J., Liu, J.R., Donnelly, J., Badylak, S.F., Modo, M., 2017. Long-term retention of ECM hydrogel after implantation into a sub-acute stroke cavity reduces lesion volume. Acta Biomater. 63, 50–63.
Ghuman, H., Massensini, A.R., Donnelly, J., Kim, S.M., Medberry, C.J., Badylak, S.F., Modo, M., 2016. ECM hydrogel for the treatment of stroke: characterization of the host cell infiltrate. Biomaterials 91, 166–181.
Ghuman, H., Mauney, C., Donnelly, J., Massensini, A.R., Badylak, S.F., Modo, M., 2018 Oct 15. Biodegradation of ECM hydrogel promotes endogenous brain tissue restoration in a rat model of stroke. Acta Biomater. 80, 66–84. https://doi.org/10.1016/j.actbio.2018.09.020. PMID: 30232030.
Goette, M.J., Keupp, J., Rahmer, J., Lanza, G.M., Wickline, S.A., Caruthers, S.D., 2015a. Balanced UTE-SSFP for 19F MR imaging of complex spectra. Magn. Reson. Med. 74, 537–543.
Goette, M.J., Lanza, G.M., Caruthers, S.D., Wickline, S.A., 2015b. Improved quantitative (19) F MR molecular imaging with flip angle calibration and B1 -mapping compensation. J. Magn. Reson. Imaging 42, 488–494.
Gong, B.Z., Gill, M., Washburn, D.B., Davenport, W.C., Adams, D., Kwock, L., 1991. Parameter optimization and calibration of 19F magnetic resonance imaging at 1.5 Tesla. Magn. Reson. Imaging 9, 101–106.
Gudbjartsson, H., Patz, S., 1995. The Rician distribution of noisy MRI data. Magn. Reson. Med. 34, 910–914.
Hitchens, T.K., Liu, L., Foley, L.M., Simplaceanu, V., Ahrens, E.T., Ho, C., 2015. Combining perfluorocarbon and superparamagnetic iron-oxide cell labeling for improved and expanded applications of cellular MRI. Magn. Reson. Med. 73, 367–375.
Hitchens, T.K., Ye, Q., Eytan, D.F., Janjic, J.M., Ahrens, E.T., Ho, C., 2011. 19F MRI detection of acute allograft rejection with in vivo perfluorocarbon labeling of immune cells. Magn. Reson. Med. 65, 1144–1153.
Hoffman, E.J., Huang, S.C., Phelps, M.E., 1979. Quantitation in positron emission computed tomography: 1. Effect of object size. J. Comput. Assist. Tomogr. 3, 299–308.
ISO, 1994. Accuracy (Trueness and Precision) of Measurement Methods and Results - Part 1: General Principles and Definitions. International Organization for Standardization, Geneva, CH, p. 17.
Jacoby, C., Temme, S., Mayenfels, F., Benoit, N., Krafft, M.P., Schubert, R., Schrader, J., Flogel, U., 2014. Probing different perfluorocarbons for in vivo inflammation imaging by 19F MRI: image reconstruction, biological half-lives and sensitivity. NMR Biomed. 27, 261–271.

Jahromi, A.H., Wang, C., Adams, S.R., Zhu, W., Narsinh, K., Xu, H., Gray, D.L., Tsien, R.Y., Ahrens, E.T., 2018. Fluorous-soluble metal chelate for sensitive fluorine-19 magnetic resonance imaging nanoemulsion probes. ACS Nano.

Janjic, J.M., Srinivas, M., Kadayakkara, D.K., Ahrens, E.T., 2008. Self-delivering nanoemulsions for dual fluorine-19 MRI and fluorescence detection. J. Am. Chem. Soc. 130, 2832–2841.

Kadayakkara, D.K., Ranganathan, S., Young, W.B., Ahrens, E.T., 2012. Assaying macrophage activity in a murine model of inflammatory bowel disease using fluorine-19 MRI. Lab. Investig. 92, 636–645.

Kessler, R.M., Ellis Jr., J.R., Eden, M., 1984. Analysis of emission tomographic scan data: limitations imposed by resolution and background. J. Comput. Assist. Tomogr. 8, 514–522.

Keupp, J., Rahmer, J., Grasslin, I., Mazurkewitz, P.C., Schaeffter, T., Lanza, G.M., Wickline, S.A., Caruthers, S.D., 2011. Simultaneous dual-nuclei imaging for motion corrected detection and quantification of 19F imaging agents. Magn. Reson. Med. 66, 1116–1122.

Kislukhin, A.A., Xu, H., Adams, S.R., Narsinh, K.H., Tsien, R.Y., Ahrens, E.T., 2016. Paramagnetic fluorinated nanoemulsions for sensitive cellular fluorine-19 magnetic resonance imaging. Nat. Mater. 15, 662–668.

Lee, H., Price, R.R., Holburn, G.E., Partain, C.L., Adams, M.D., Cacheris, W.P., 1994. In vivo fluorine-19 MR imaging: relaxation enhancement with Gd-DTPA. J. Magn. Reson. Imaging 4, 609–613.

Liang, S., Dresselaers, T., Louchami, K., Zhu, C., Liu, Y., Himmelreich, U., 2017. Comparison of different compressed sensing algorithms for low SNR (19) F MRI applications-Imaging of transplanted pancreatic islets and cells labeled with perfluorocarbons. NMR Biomed. 30.

LoPresti, S.T., Brown, B.N., 2018. Effect of source animal age upon macrophage response to extracellular matrix biomaterials. J Immunol Regen Med 1, 57–66.

Markevich, N., Gertner, I., 1989. Comparison among methods for calculating FWHM. Nucl. Instrum. Methods Phys. Res. A283, 72–77.

Massensini, A.R., Ghuman, H., Saldin, L.T., Medberry, C.J., Keane, T.J., Nicholls, F.J., Velankar, S.S., Badylak, S.F., Modo, M., 2015. Concentration-dependent rheological properties of ECM hydrogel for intracerebral delivery to a stroke cavity. Acta Biomater. 27, 116–130.

Mastropietro, A., De Bernardi, E., Breschi, G.L., Zucca, I., Cametti, M., Soffientini, C.D., de Curtis, M., Terraneo, G., Metrangolo, P., Spreafico, R., Resnati, G., Baselli, G., 2014. Optimization of rapid acquisition with relaxation enhancement (RARE) pulse sequence parameters for (1)(9)F-MRI studies. J. Magn. Reson. Imaging 40, 162–170.

Medberry, C.J., Crapo, P.M., Siu, B.F., Carruthers, C.A., Wolf, M.T., Nagarkar, S.P., Agrawal, V., Jones, K.E., Kelly, J., Johnson, S.A., Velankar, S.S., Watkins, S.C., Modo, M., Badylak, S.F., 2013. Hydrogels derived from central nervous system extracellular matrix. Biomaterials 34, 1033–1040.

Meissner, M., Reisert, M., Hugger, T., Hennig, J., von Elverfeldt, D., Leupold, J., 2015. Revealing signal from noisy (19) F MR images by chemical shift artifact correction. Magn. Reson. Med. 73, 2225–2233.

Modo, M., Hoehn, M., Bulte, J.W., 2005. Cellular MR imaging. Mol. Imaging 4, 143–164.

Modo, M., Stroemer, R.P., Tang, E., Veizovic, T., Sowniski, P., Hodges, H., 2000. Neurological sequelae and long-term behavioural assessment of rats with transient middle cerebral artery occlusion. J. Neurosci. Methods 104, 99–109.

Nitz, W.R., 2002. Fast and ultrafast non-echo-planar MR imaging techniques. Eur. Radiol. 12, 2866–2882.

Ogle, M.E., Segar, C.E., Sridhar, S., Botchwey, E.A., 2016. Monocytes and macrophages in tissue repair: implications for immunoregenerative biomaterial design. Exp. Biol. Med. 241, 1084–1097.

Ogura, A., Maeda, F., Miyai, A., Kikumoto, R., 2005. [Effects of slice thickness and matrix size on MRI for signal detection]. Nippon. Hoshasen Gijutsu Gakkai Zasshi 61, 1140–1143.

Partlow, K.C., Chen, J., Brant, J.A., Neubauer, A.M., Meyerrose, T.E., Creer, M.H., Nolta, J.A., Caruthers, S.D., Lanza, G.M., Wickline, S.A., 2007. 19F magnetic resonance imaging for stem/progenitor cell tracking with multiple unique perfluorocarbon nanobeacons. FASEB J. Off. Publ. Fed. Am. Soc. Exp. Biol. 21, 1647–1654.

Rahmim, A., Qi, J., Sossi, V., 2013. Resolution modeling in PET imaging: theory, practice, benefits, and pitfalls. Med. Phys. 40, 064301.

Ratner, A.V., Hurd, R., Muller, H.H., Bradley-Simpson, B., Pitts, W., Shibata, D., Sotak, C., Young, S.W., 1987. 19F magnetic resonance imaging of the reticuloendothelial system. Magn. Reson. Med. 5, 548–554.

Robson, M.D., Gore, J.C., Constable, R.T., 1997. Measurement of the point spread function in MRI using constant time imaging. Magn. Reson. Med. 38, 733–740.

Schmid, F., Holtke, C., Parker, D., Faber, C., 2013. Boosting (19) F MRI-SNR efficient detection of paramagnetic contrast agents using ultrafast sequences. Magn. Reson. Med. 69, 1056–1062.

Smith, S.W., 1997. The Scientist and Engineer's Guide to Digital Signal Processing. California Technical Publishing, San Diego, CA.

Srinivas, M., Morel, P.A., Ernst, L.A., Laidlaw, D.H., Ahrens, E.T., 2007. Fluorine-19 MRI for visualization and quantification of cell migration in a diabetes model. Magn. Reson. Med. 58, 725–734.

Stille, M., Smith, E.J., Crum, W.R., Modo, M., 2013. 3D reconstruction of 2D fluorescence histology images and registration with in vivo MR images: application in a rodent stroke model. J. Neurosci. Methods 219, 27–40.

Taylor, A.J., Granwehr, J., Lesbats, C., Krupa, J.L., Six, J.S., Pavlovskaya, G.E., Thomas, N.R., Auer, D.P., Meersmann, T., Faas, H.M., 2016. Probe-specific procedure to estimate sensitivity and detection limits for 19F magnetic resonance imaging. PLoS One 11 e0163704.

Temme, S., Bonner, F., Schrader, J., Flogel, U., 2012. 19F magnetic resonance imaging of endogenous macrophages in inflammation. Wiley. Interdiscip. Rev. Nanomed. Nanobiotechnol. 4, 329–343.

Tirotta, I., Mastropietro, A., Cordiglieri, C., Gazzera, L., Baggi, F., Baselli, G., Bruzzone, M.G., Zucca, I., Cavallo, G., Terraneo, G., Baldelli Bombelli, F., Metrangolo, P., Resnati, G., 2014. A superfluorinated molecular probe for highly sensitive in vivo(19)F-MRI. J. Am. Chem. Soc. 136, 8524–8527.

Valentin, J.E., Stewart-Akers, A.M., Gilbert, T.W., Badylak, S.F., 2009. Macrophage participation in the degradation and remodeling of extracellular matrix scaffolds. Tissue Eng. A 15, 1687–1694.

Waiczies, H., Lepore, S., Drechsler, S., Qadri, F., Purfurst, B., Sydow, K., Dathe, M., Kuhne, A., Lindel, T., Hoffmann, W., Pohlmann, A., Niendorf, T., Waiczies, S., 2013. Visualizing brain inflammation with a shingled-leg radio-frequency head probe for 19F/1H MRI. Sci. Rep. 3, 1280.

Waiczies, S., Millward, J.M., Starke, L., Delgado, P.R., Huelnhagen, T., Prinz, C., Marek, D., Wecker, D., Wissmann, R., Koch, S.P., Boehm-Sturm, P., Waiczies, H., Niendorf, T., Pohlmann, A., 2017. Enhanced fluorine-19 MRI sensitivity using a cryogenic radiofrequency probe: technical developments and ex vivo demonstration in a mouse model of neuroinflammation. Sci. Rep. 7, 9808.

Welvaert, M., Rosseel, Y., 2013. On the definition of signal-to-noise ratio and contrast-to-noise ratio for FMRI data. PLoS One 8 e77089.

Zhong, J., Mills, P.H., Hitchens, T.K., Ahrens, E.T., 2013a. Accelerated fluorine-19 MRI cell tracking using compressed sensing. Magn. Reson. Med. 69, 1683–1690.

Zhong, J., Narsinh, K., Morel, P.A., Xu, H., Ahrens, E.T., 2015. In vivo quantification of inflammation in experimental autoimmune encephalomyelitis rats using fluorine-19 magnetic resonance imaging reveals immune cell recruitment outside the nervous system. PLoS One 10 e0140238.

Zhong, J., Sakaki, M., Okada, H., Ahrens, E.T., 2013b. In vivo intracellular oxygen dynamics in murine brain glioma and immunotherapeutic response of cytotoxic T cells observed by fluorine-19 magnetic resonance imaging. PLoS One 8 e59479.